Supplementary Information for

Dual Interfacial Hydrogen Bonds Enable Efficient Deep-Blue LEDs Based on a Hybrid Copper Iodide

Kun Zhu[1,2], Obadiah Reid[3], Sylvie Rangan[2], Kang Zhou[4], Nasir Javed[5], Leila Kasaei[2], Chongqing Yang[6], Mingxing Li[7], Yue Sun[1], Mircea Cotlet[7], Yi Liu[6], Leonard C. Feldman[2], Deirdre M. O'Carroll[1,5], Kai Zhu[3], Jing Li[1*]

[1] Dr. Kun Zhu, Yue Sun, Prof. Deirdre M. O'Carroll, Prof. Jing Li
Department of Chemistry and Chemical Biology, Rutgers University
123 Bevier Road, Piscataway, NJ 08854, USA
E-mail: Jingli@rutgers.edu

[2] Dr. Kun Zhu, Prof. Sylvie Rangan, Dr. Leila Kasaei, Prof. Leonard C. Feldman
Department of Physics and Astronomy, Rutgers University
136 Frelinghuysen Rd, Piscataway Township, NJ 08854, USA

[3] Dr. Obadiah Reid, Dr. Kai Zhu
National Renewable Energy Laboratory,
15013 Denver West Parkway, Golden, Colorado 80401, United States

[4] Dr. Kang Zhou
Hoffmann Institute of Advanced Materials, Shenzhen Polytechnic,
7098 Liuxian Boulevard, Shenzhen, Guangdong 518055, P. R. China

[5] Nasir Javed, Prof. Deirdre M. O'Carroll
Department of Materials Science and Engineering, Rutgers University
607 Taylor Road, Piscataway, NJ 08854, USA

[6] Dr. Chongqing Yang, Prof. Yi Liu
The Molecular Foundry, Lawrence Berkeley National Laboratory,
67 Cyclotron Rd, Berkeley, CA, 94720 USA

[7] Dr. Mingxing Li, Dr. Mircea Cotlet
Center for Functional Nanomaterials, Brookhaven National Laboratory

98 Rochester Street, Upton, NY 11973, USA

Additional crystallographic data

Table. S1. Crystallographic data of 1D-Cu_4I_8(*Hdabco*)$_4$ obtained from SCXRD.

Compound	1D-Cu_4I_8(*Hdabco*)$_4$
Empirical Formula	C6 H13 Cu2 I4 N2
Formula weight	861.07
Temperature	298 K
Wavelength	0.71073
Crystal system	Orthorhombic
Space Group	Pnma
Unit cell dimensions	a = 13.6210(5) Å α = 90.0° b = 10.0312(3) Å β = 90.0° c = 15.5034(6) Å γ = 90.0°
Volume	2118.31(13) $Å^3$
Z	4
Density	2.700 Mg/m^3
Absorption coefficient	7.839 mm^{-1}
F(000)	1584.0
Theta (max)	27.490°
h, k, lmax	17, 13, 20
Reflections collected	2564
Completeness to theta = 31.444°	0.998
Absorption correction	MULTI-SCAN
Max. and min. transmission	0.574 and 0.625
R_1	0.0362
wR_2	0.0791

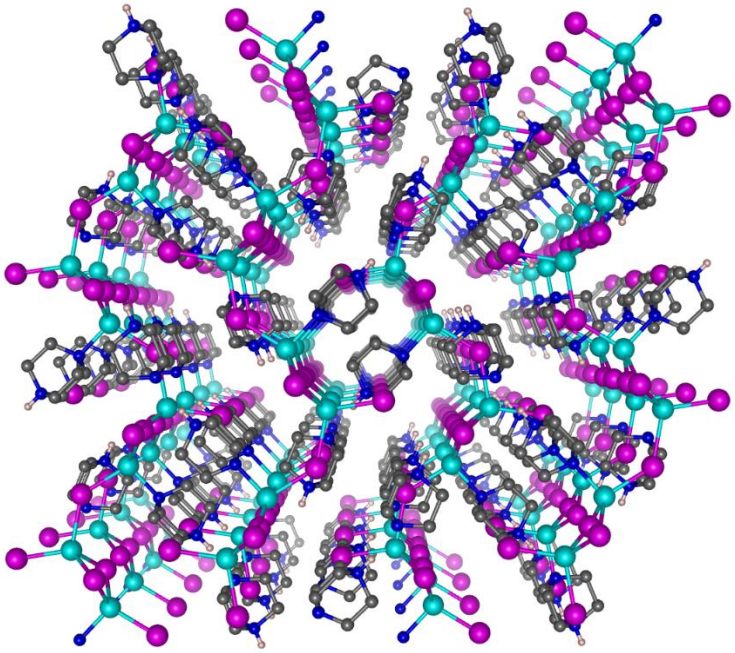

Fig. S1. Perspective view of the crystal structure of 1D-Cu_4I_8(*Hdabco*)$_4$ along *b*-axis (top).

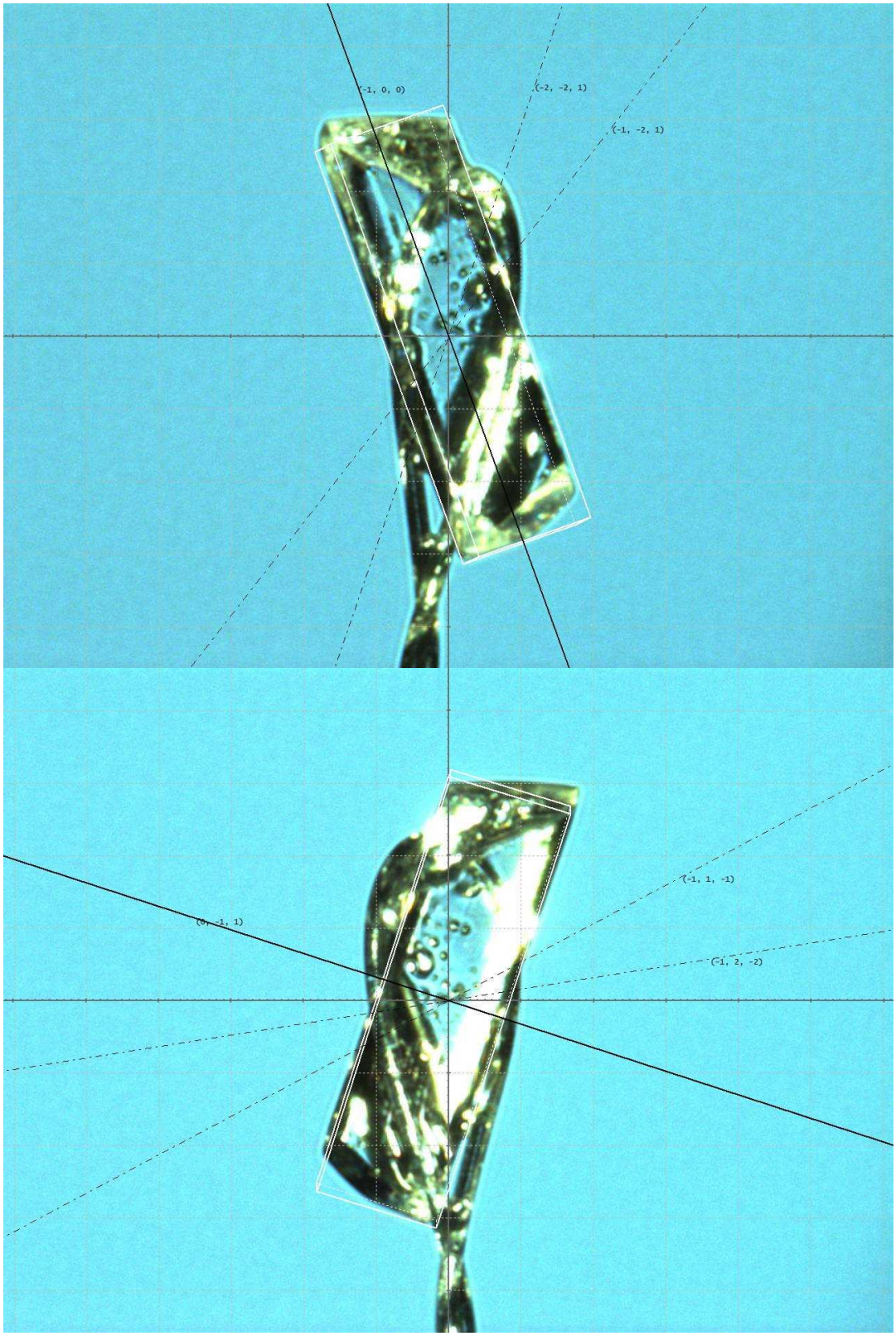

Fig. S2. Crystal images and faces measured by SCXRD on a rod-like 1D-Cu_4I_8(*Hdabco*)$_4$ single crystal.

Additional surface morphology data

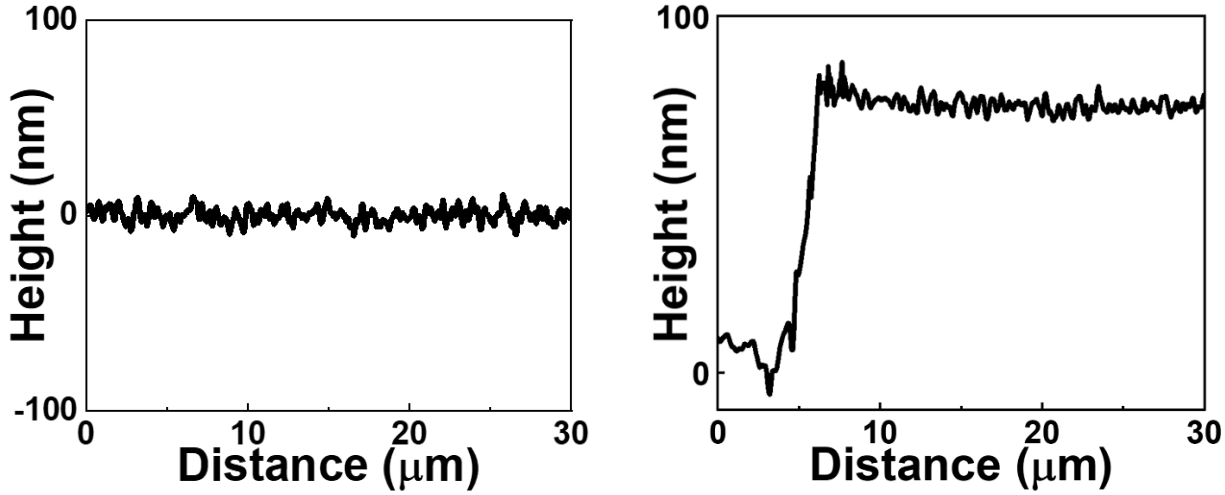

Fig. S3. AFM surface (left) and thickness (right) profile of a~~n~~ scratched CuI(*Hda*) thin film on ITO.

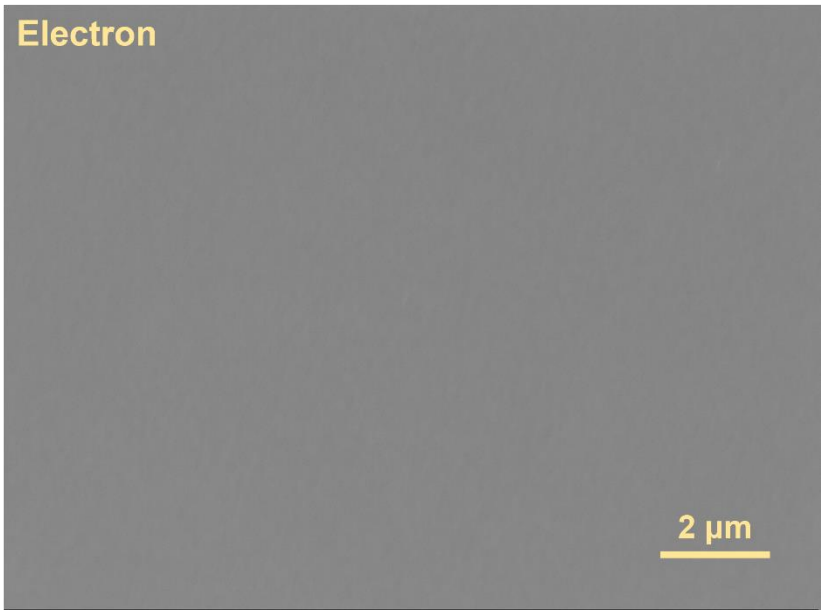

Fig. S4. Top-view of the SEM image of an as-made CuI(*Hda*) thin film on ITO.

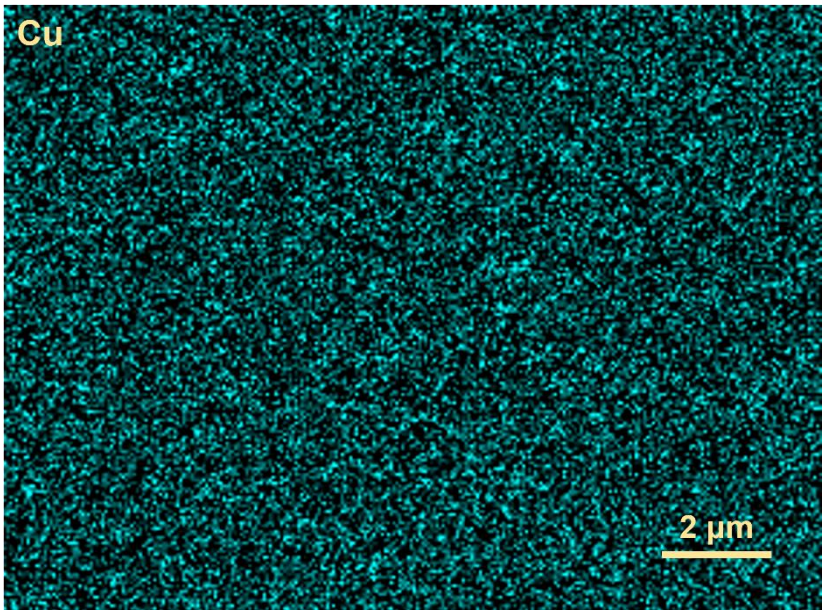

Fig. S5. Elemental mapping of Cu by energy dispersive spectroscopy (EDS) of the same CuI(*Hda*) thin film.

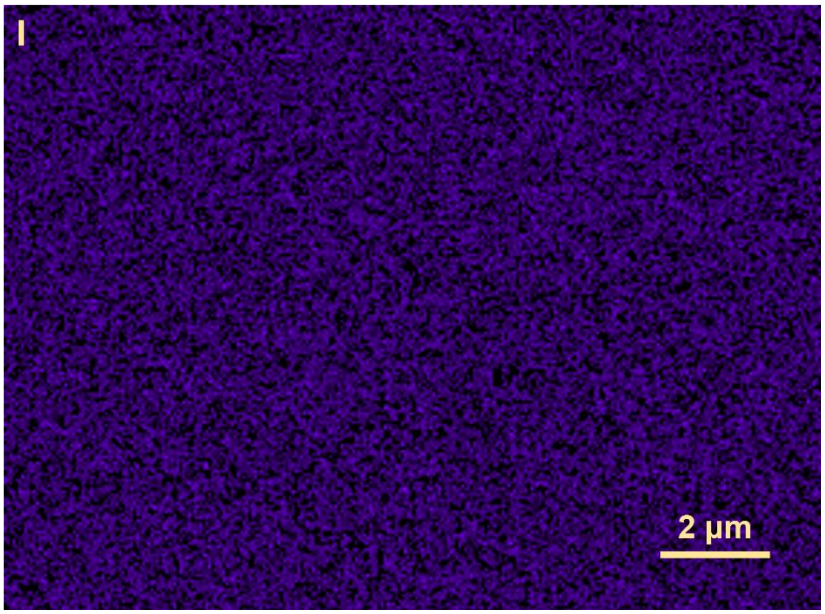

Fig. S6. Elemental mapping of I by energy dispersive spectroscopy (EDS) of the same CuI(*Hda*) thin film.

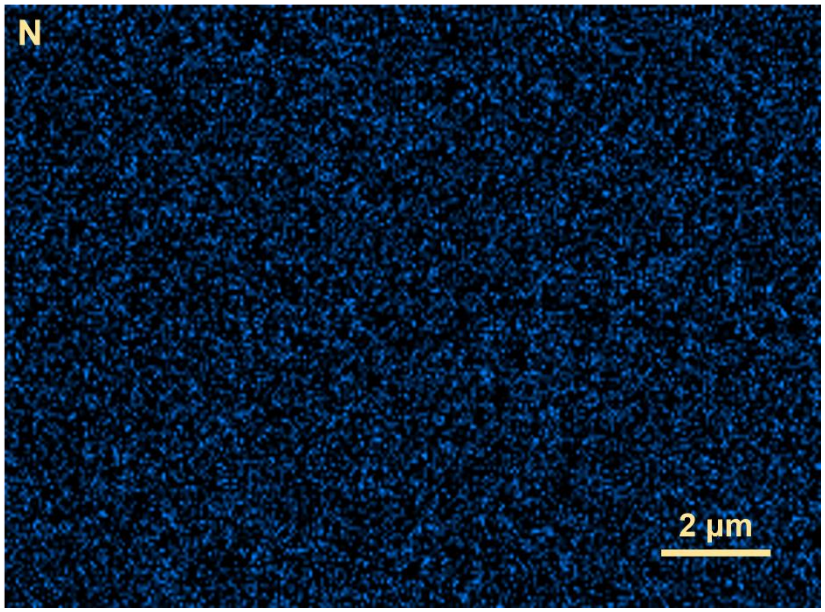

Fig. S7. Elemental mapping of N by energy dispersive spectroscopy (EDS) of the same CuI(*Hda*) thin film.

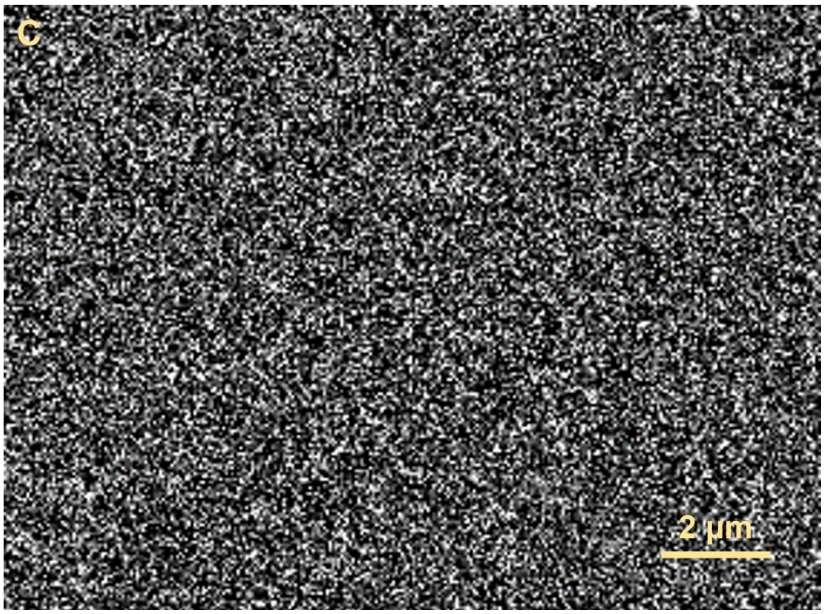

Fig. S8. Elemental mapping of I by energy dispersive spectroscopy (EDS) of the same CuI(*Hda*) thin film.

Additional 1D line-cut GIWAXS profiles

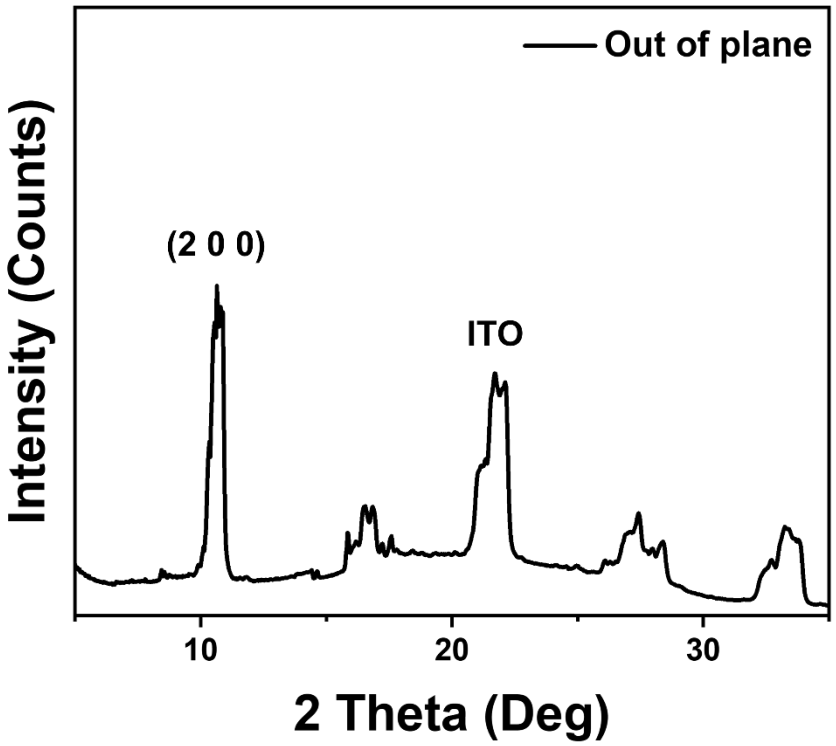

Fig. S9. 1D GIWAXS out-of-plane pattern of a CuI(*Hda*) thin film (90 nm) on ITO.

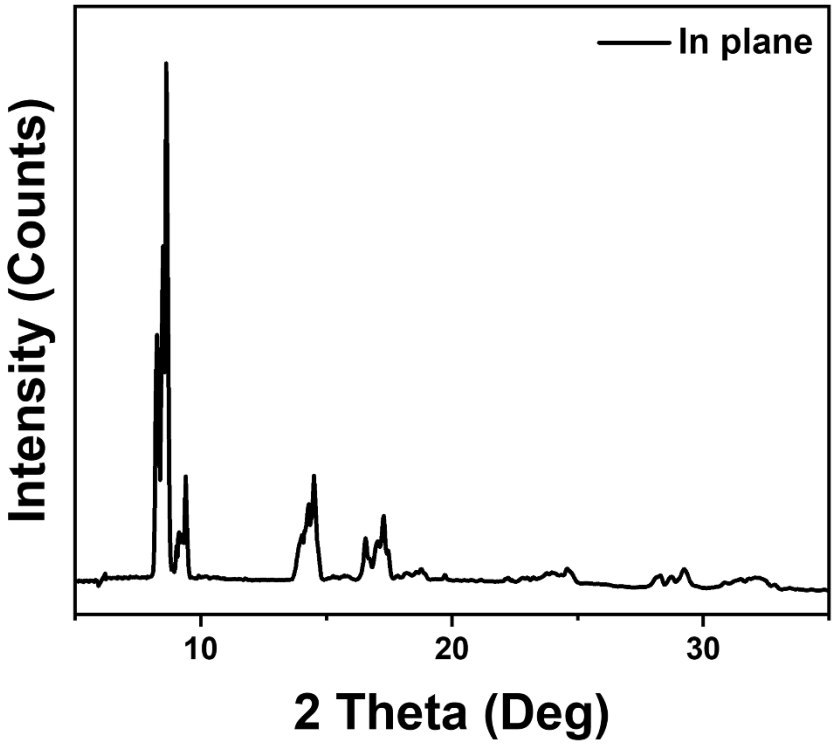

Fig. S10. 1D GIWAXS in-plane pattern of a CuI(*Hda*) thin film (90 nm) on ITO.

PLQY of CuI(*Hda*)

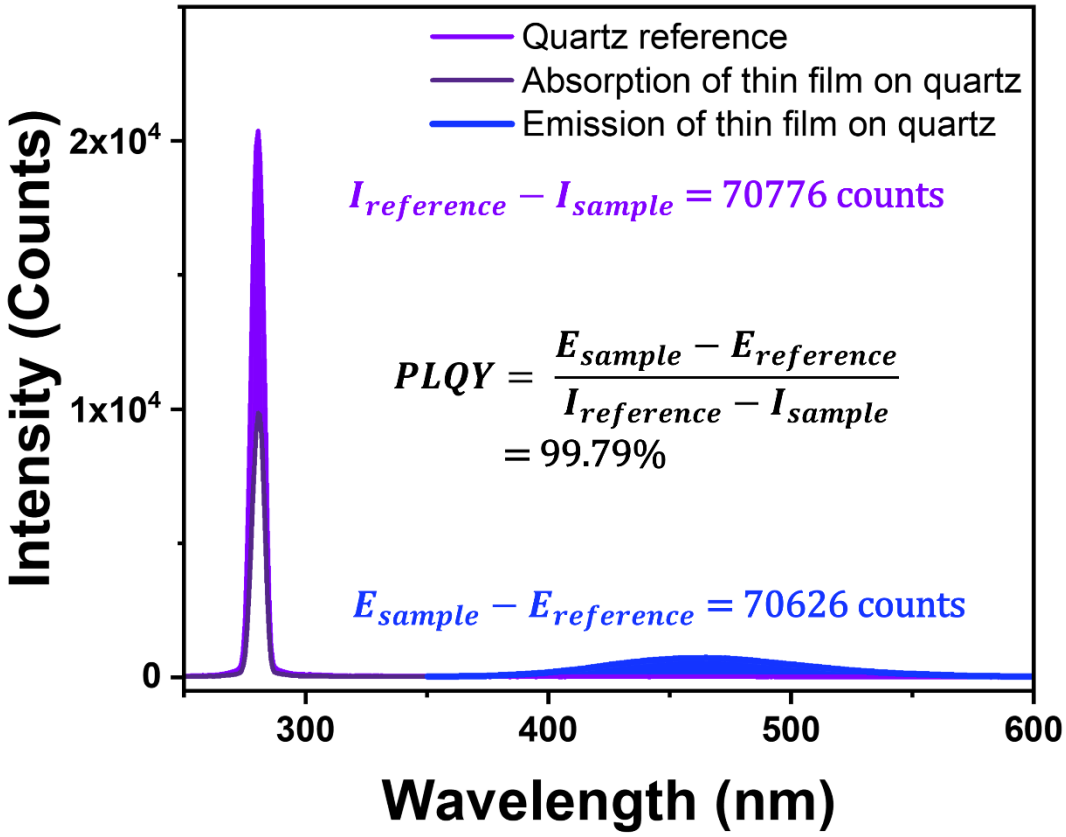

Fig. S11. PLQY analysis of a CuI(*Hda*) polycrystalline thin film on quartz which yielded a near-unity quantum efficiency.

Summary of TRPL lifetime of CuI(*Hda*) fitted at different temperature and radiative/non-radiative decay constants

Table S2. Summary of lifetime values of CuI(*Hda*) obtained at various temperatures.

Temp (K)	**Fraction$_1$**	**τ_1 (µs)**	**Fraction$_2$**	**τ_2 (µs)**	**Fraction$_3$**	**τ_3 (µs)**	**τ_{av}/int (µs)**
78	0.66%	0.032	14.49%	1.056	84.85%	6.742	5.874
100	0.65%	0.030	14.22%	1.027	85.13%	6.693	5.855
125	0.55%	0.023	14.03%	0.959	85.41%	6.681	5.841
150	0.56%	0.020	14.40%	0.923	85.04%	6.466	5.632
175	0.61%	0.019	14.10%	0.863	85.29%	6.113	5.335
200	0.64%	0.018	14.62%	0.837	84.74%	5.802	5.039
225	0.68%	0.017	15.13%	0.818	84.19%	5.528	4.778
250	0.74%	0.017	15.49%	0.769	83.77%	5.237	4.506
275	0.81%	0.016	16.75%	0.726	82.44%	4.889	4.152
298	0.93%	0.016	18.74%	0.691	80.34%	4.468	3.719
298-BC	0.94%	0.015	19.93%	0.614	79.13%	3.963	3.259

int = intensity weighted. BC = before cooling

Supplementary note 1.

To quantitatively assess and compare the degree of radiative and non-radiative contributions, total radiative rate (k_r) and non-radiative decay rate (k_{nr}) were estimated based on Equation. S1 and S2.

$$\eta_{PL} = k_r / (k_r + k_{nr}) \quad \text{(S1)}$$

$$\tau_{PL} = 1 / (k_r + k_{nr}) \quad \text{(S2)}$$

where η_{PL} is the PLQY value and τ_{PL} is the average PL lifetime. The k_r of CuI(*Hda*) at 298K was calculated to be 3.05×10^5 s^{-1}, which is more than two orders of magnitude higher than that of k_{nr}(1.84×10^3 s^{-1}).

Power-dependent photoluminescent spectra of CuI(*Hda*)

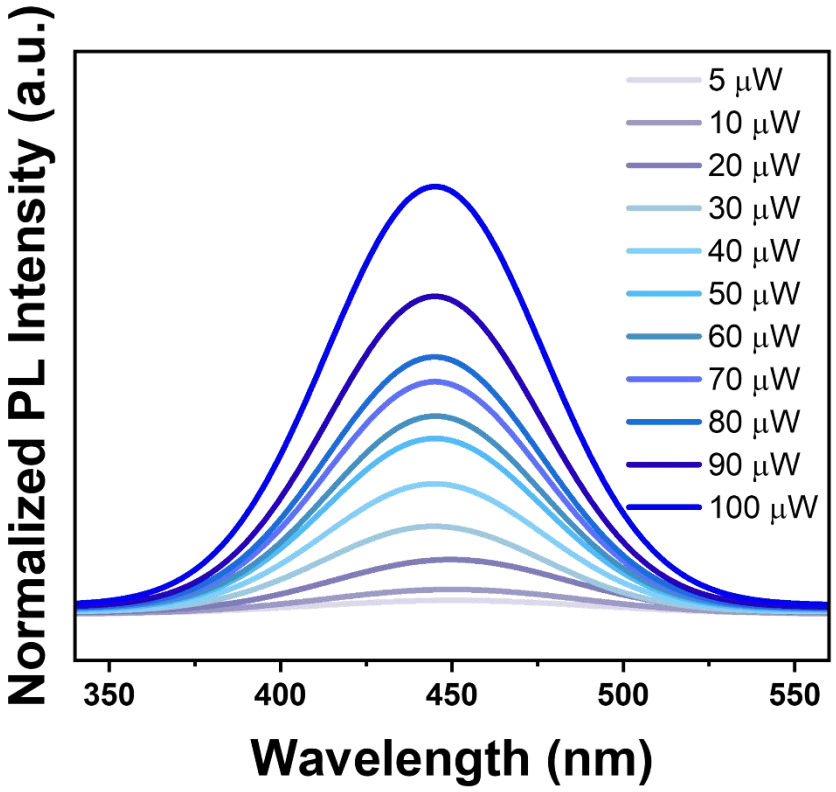

Fig. S12. Power-dependent PL spectra of a CuI(*Hda*) thin film (90 nm) under 280 nm excitation.

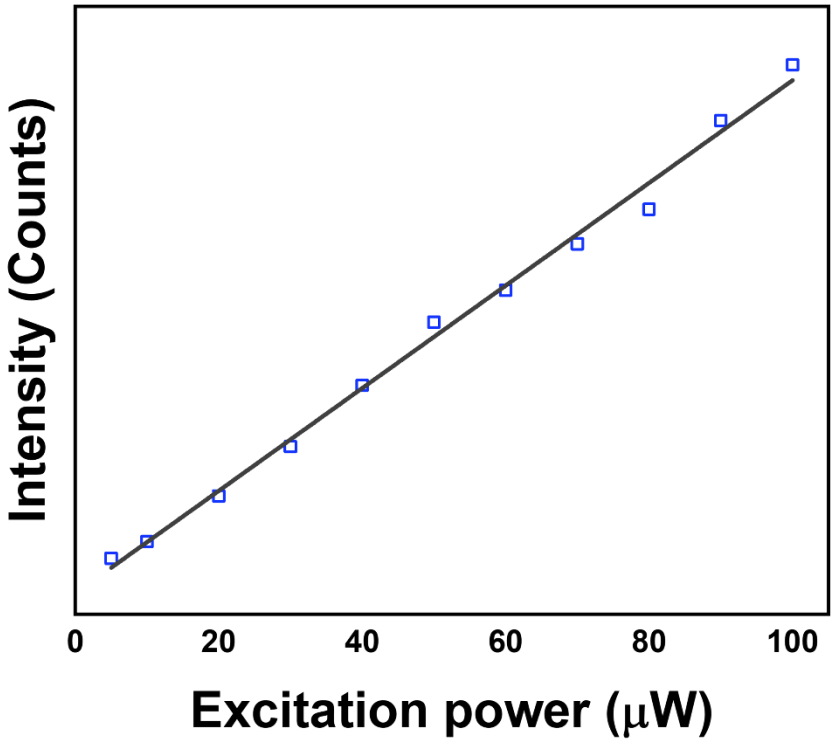

Fig. S13. Linear fitting of the power-dependent PL spectra.

Supplementary note 2. Detail analysis of temperature dependent steady state PL

Extremely low Huang−Rhys factor (*S*) and photon frequency ($\hbar\omega_{\text{photon}}$) could be fitted from Equation. S3.

$$FWHM = 2.36\sqrt{S}\hbar\omega_{\text{photon}}\sqrt{coth\frac{\hbar\omega_{\text{photon}}}{2k_BT}} \quad \text{(S3)}$$

The exciton binding energy was fitted following Equation. S4:

$$I(T) = \frac{I_0}{1+Aexp(-\frac{E_b}{k_BT})} \quad \text{(S4)}$$

Where I_0 is the integrated PL intensity at 0 K, E_b is the exciton binding energy, k_B is the Boltzmann's constant and A is a constant.

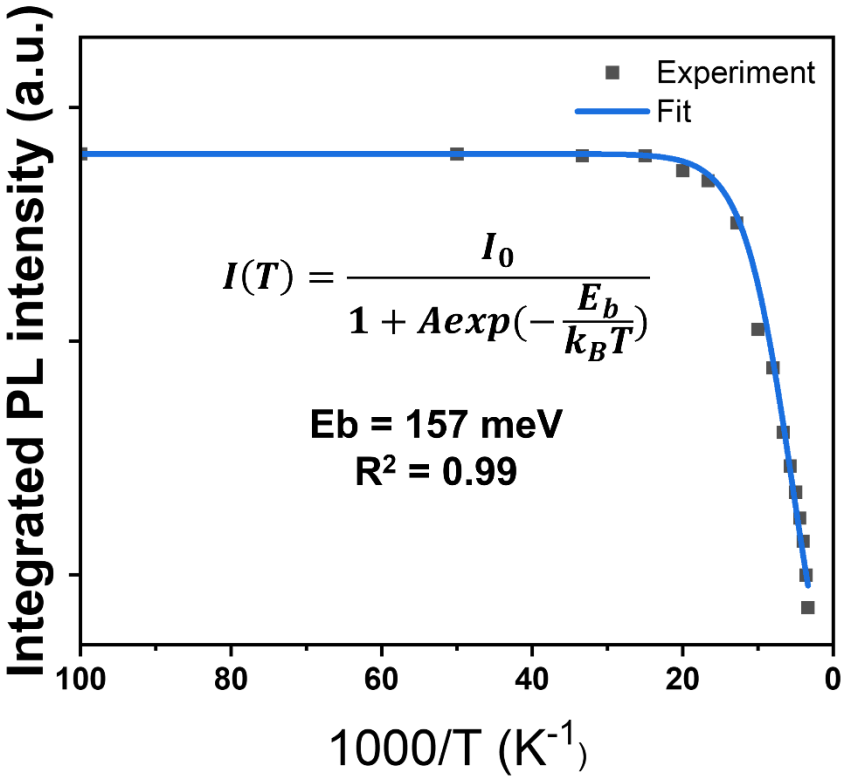

Fig. S14. Integrated PL intensity of CuI(*Hda*) as a function of reciprocal of temperature from 10 to 298 K.

Supplementary note 3. Detail analysis of TA spectroscopies

In the 2D fs-TA mapping, a strong ground state bleaching peak centered at 381 and an excited state absorption band appears in the red spectral region with a broad peak evolving from 601 nm towards 624 nm with delay time following optical pumping, which accounts for a rather small energy shift (about 76 meV).

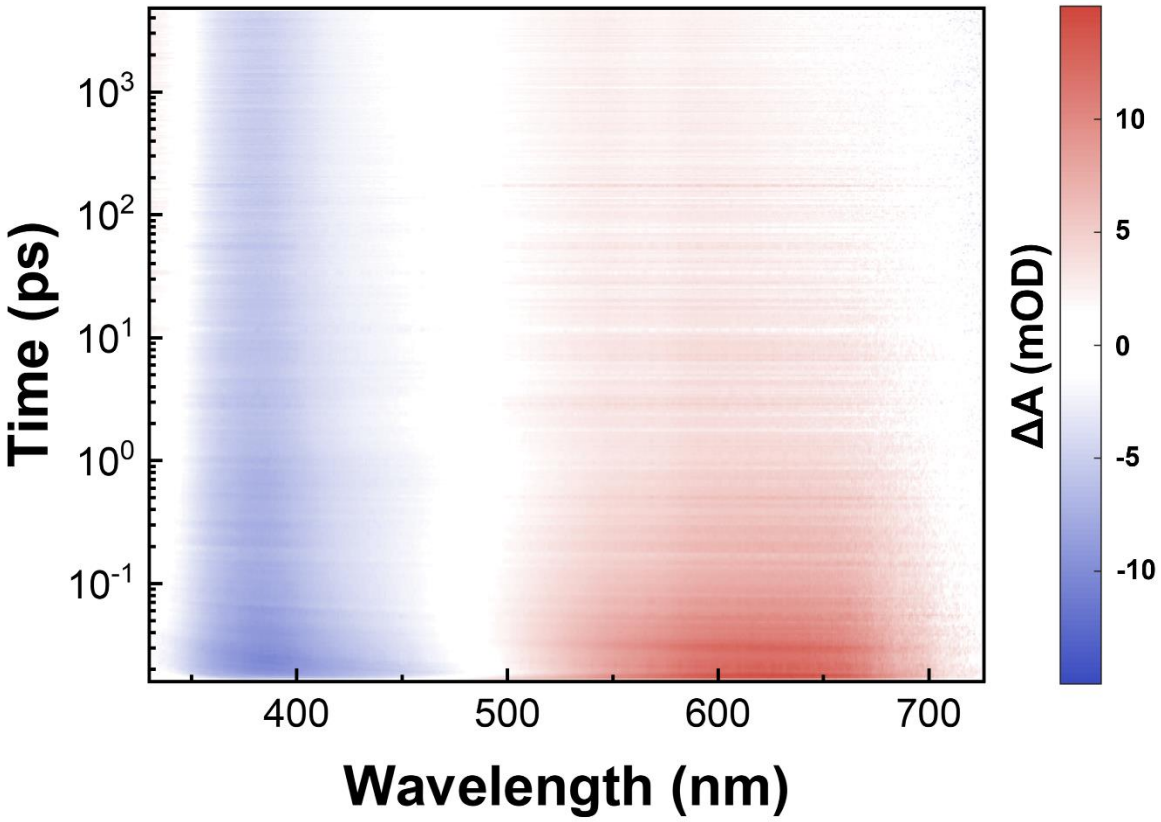

Fig. S15. Pseudocolor fs-TA plot of the sample showing the evolution of two ΔA bands (A:absorbance).

The ground state bleaching and excited state absorption peaks could be described by quadric- and tri-exponential decay fits, respectively. Four decay constants of the ground state bleaching of 8.5 ps, 13.5 ns, 59.2 ns and 4.8 μs, could be distinguished as vibrational relaxation (VR), fluorescence, TADF and phosphorescence by their timescale. The tri-exponential decay process of the excited state absorption band at ~612 nm could be fitted by time constants of 684 fs, 41.4 ps and 2.7 ns. The fastest decay process with sub-picosecond timescale could be assigned as internal vibration relaxation of the S_1 state, accounting for the small red shift of the peak position. The picosecond time constant (41.4 ps) could be explained by the depopulation of S_1, following S_1-S_n absorption, through intersystem crossing (ISC) to the triplet state. The slowest decay constant (2.7 ns) is at comparable timescale as the fluorescence decay lifetime in both TRPL and ground state bleaching peak, strongly suggesting the fluorescence decay path in CuI(*Hda*) blue emitter.

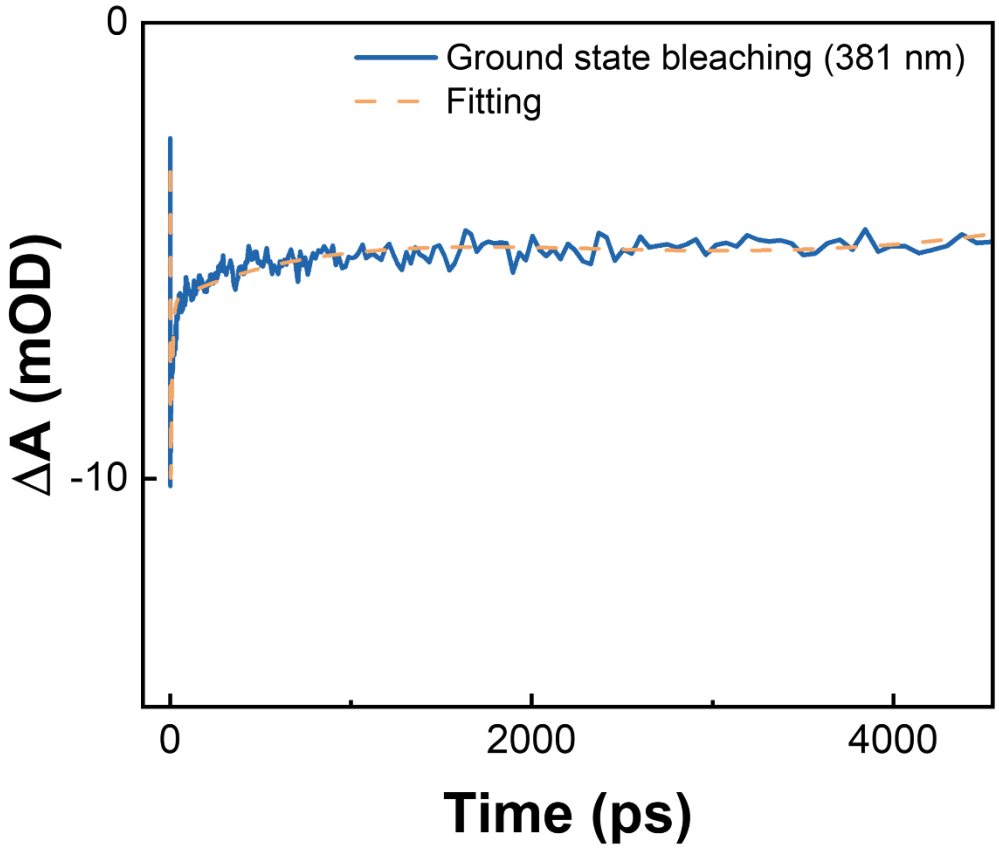

Fig. S16. Quadric-exponential fitting of the fs-TA decay of CuI(*Hda*) probed at 381 nm.

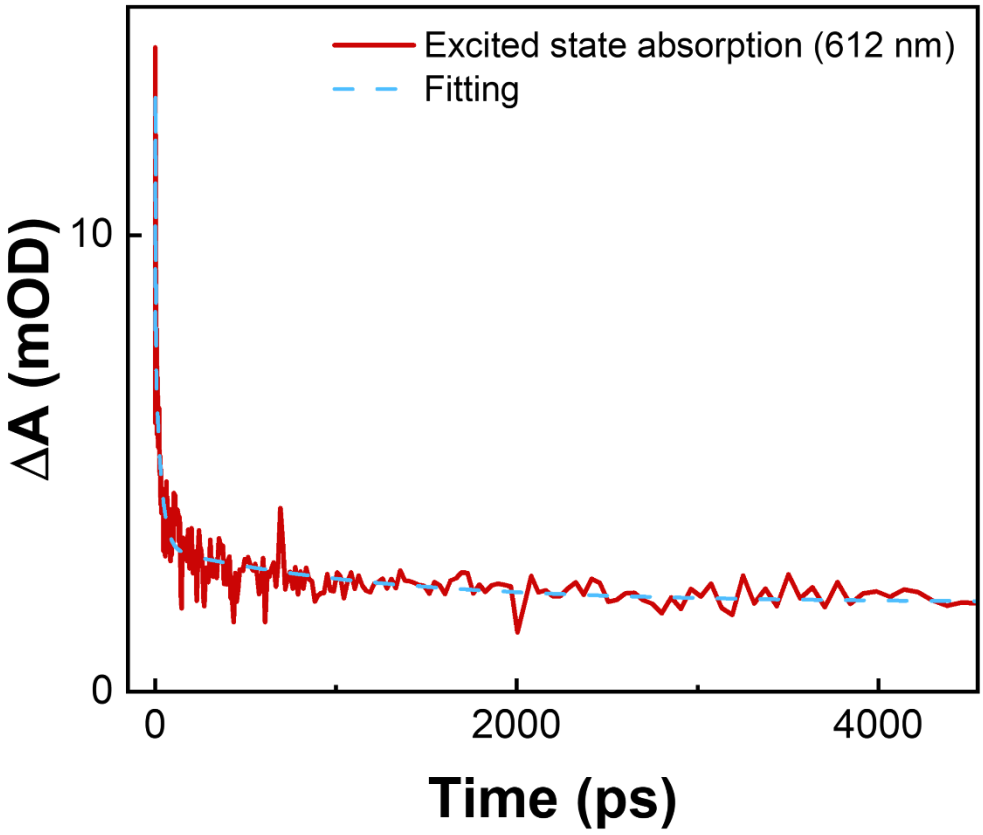

Fig. S17. Tri-exponential fitting of the fs-TA decay of CuI(*Hda*) probed at 612 nm.

Table S3. Summary of the amplitudes and time constants of the fs-TA fitting of ground state bleaching band at 381 nm.

A_1	τ_1	A_2	τ_2	A_3	τ_3	A_4	τ_4
-5.65E-3	8.5 ps	-6.64E-2	13.5 ns	-4.71E1	59.2 ns	-1.61E2	4.9 μs

Table S4. Summary of the amplitudes and time constants of the fs-TA fitting of excited state absorption band at 612 nm.

A_1	τ_1	A_2	τ_2	A_3	τ_3
4.132E+0	684 fs	4.347E-3	41.4 ps	1.201E-3	2.7 ns

It's important to note that the fs-TA's pump and probe have a maximum delay time of 4.5 ns, meaning that any decay constants longer than this timescale can only be accurately determined in terms of their magnitude, but not with precise numerical values. To obtain a quantitative and precise decay constant, ns-TA was conducted parallelly on thin-film samples of CuI(*Hda*). Same bleaching band located at 381 nm is observed, with a more comparable tri-exponential fitting of 32.68 ns, 107.49 ns and 5.40 μs to the TRPL results.

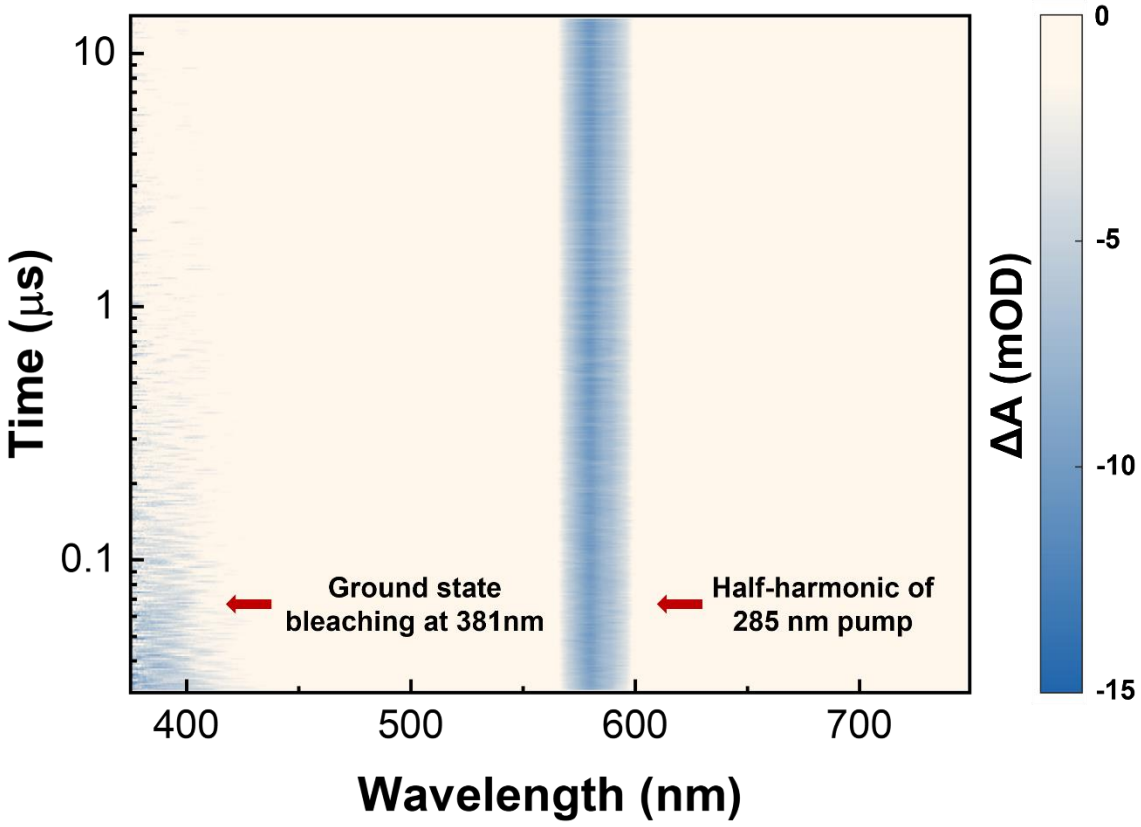

Fig. S18. Pseudocolor plot of the ns-TA plot of CuI(*Hda*).

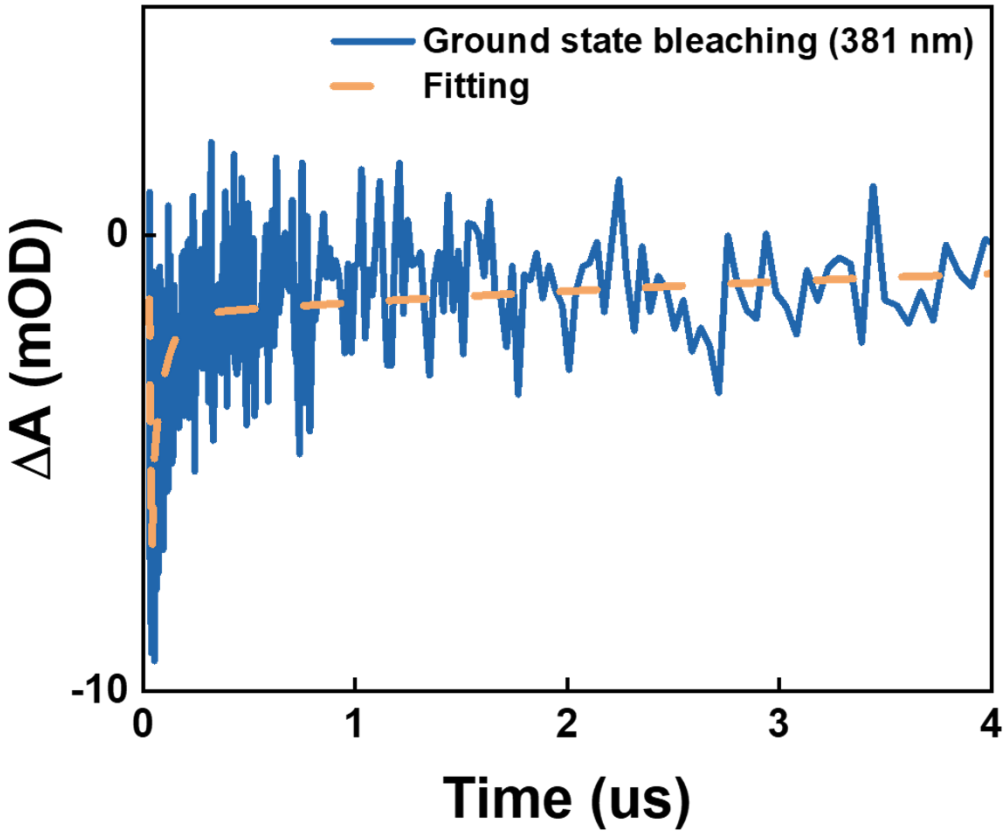

Fig. S19. Tri-exponential fitting of the ground bleaching band in ns-TA at 381 nm.

Table S5. Summary of the amplitudes and time constants of the ns-TA fitting of ground state bleaching band at 381 nm.

A_1	τ_1	A_2	τ_2	A_3	τ_3
-5.124E-1	32.68 ns	-6.644E-3	107.49 ns	-1.771E-3	5.396 μs

X-ray photoelectron spectroscopy (XPS), Ultraviolet photoelectron spectroscopy (UPS) and reflected electron energy loss spectroscopy (REELS) data of CuI(*Hda*) thin film

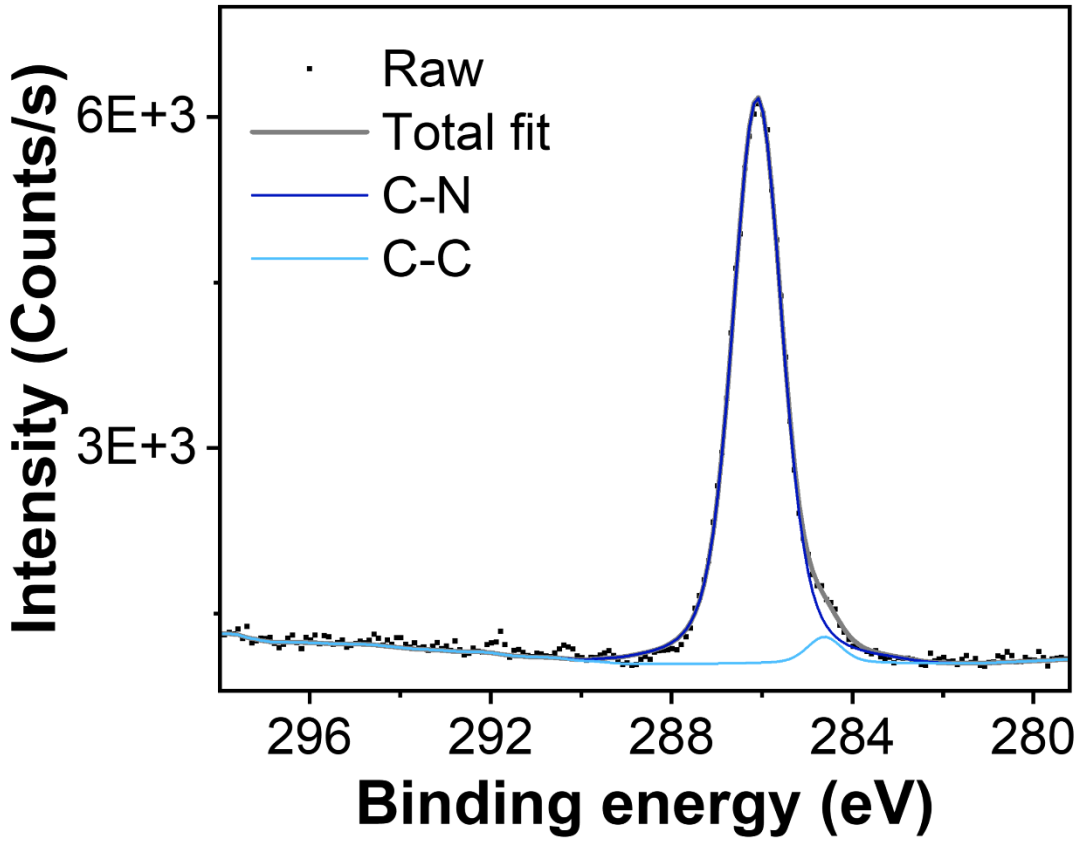

Fig. S20. XPS C1s core level spectrum of a CuI(*Hda*) thin film.

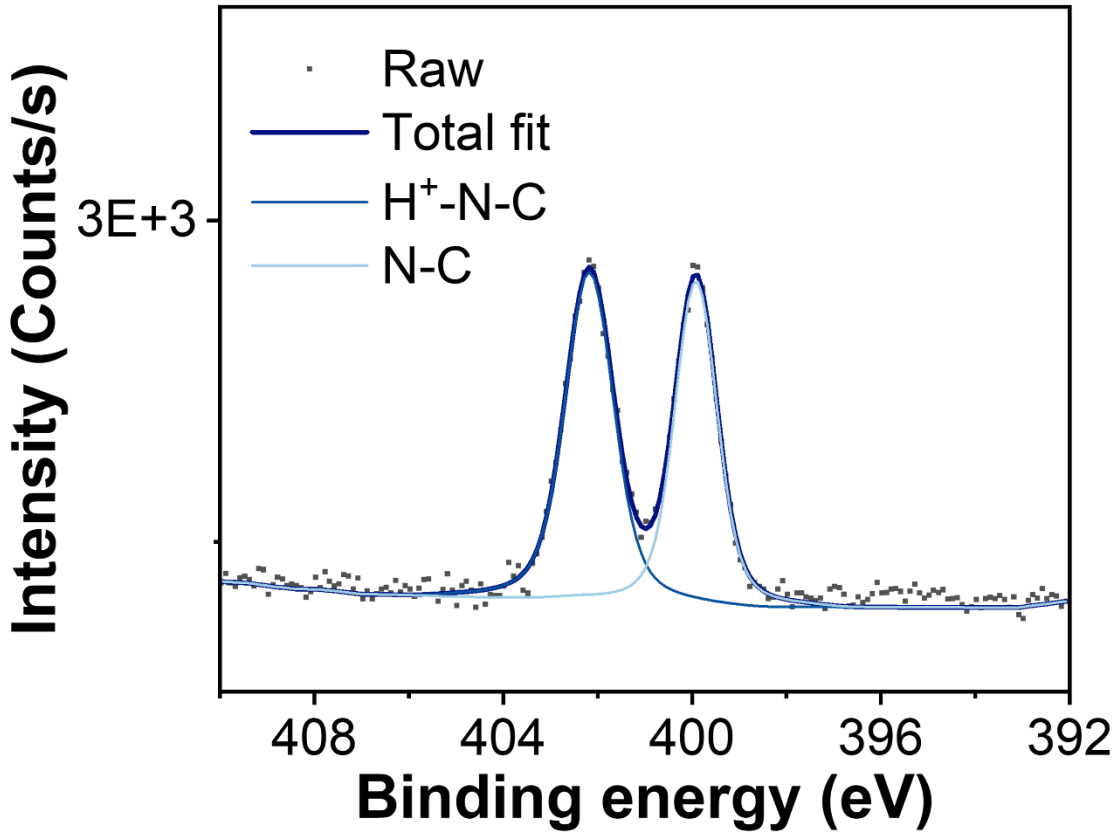

Fig. S21. XPS N1s core level spectrum of a CuI(*Hda*) thin film.

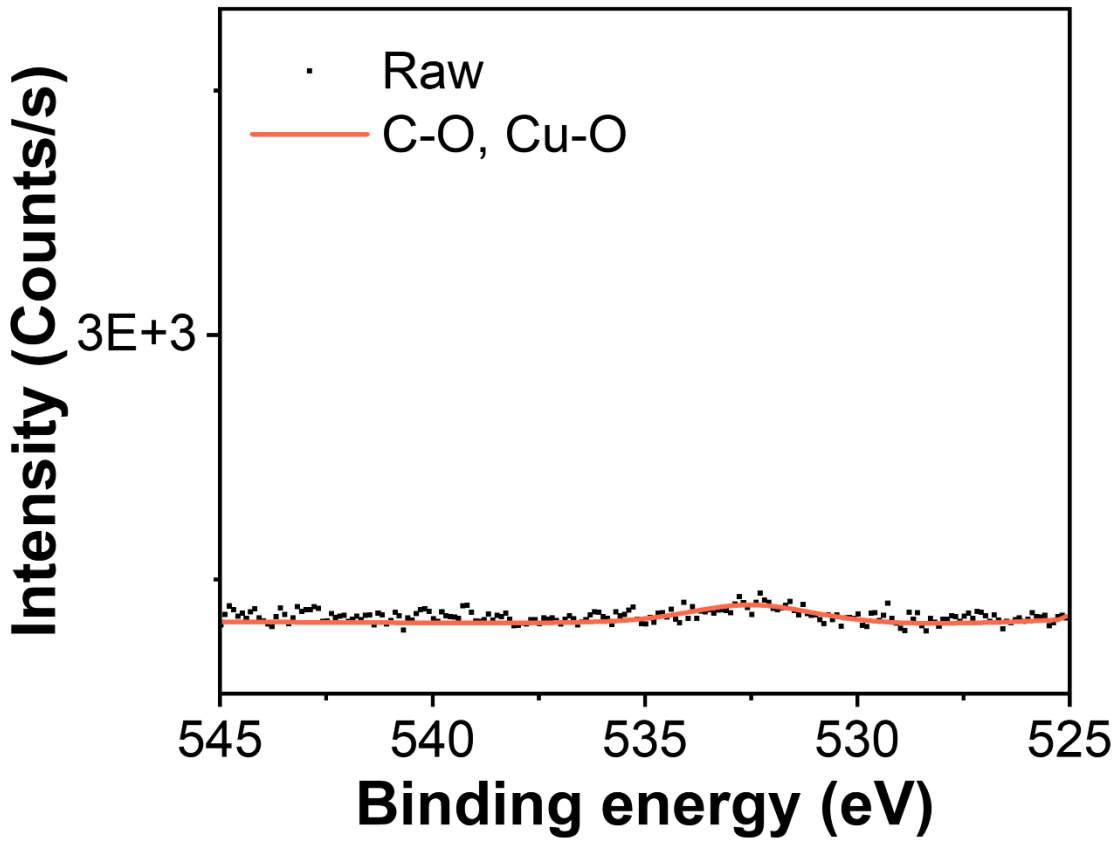

Fig. S22. XPS O1s core level spectrum of a CuI(*Hda*) thin film.

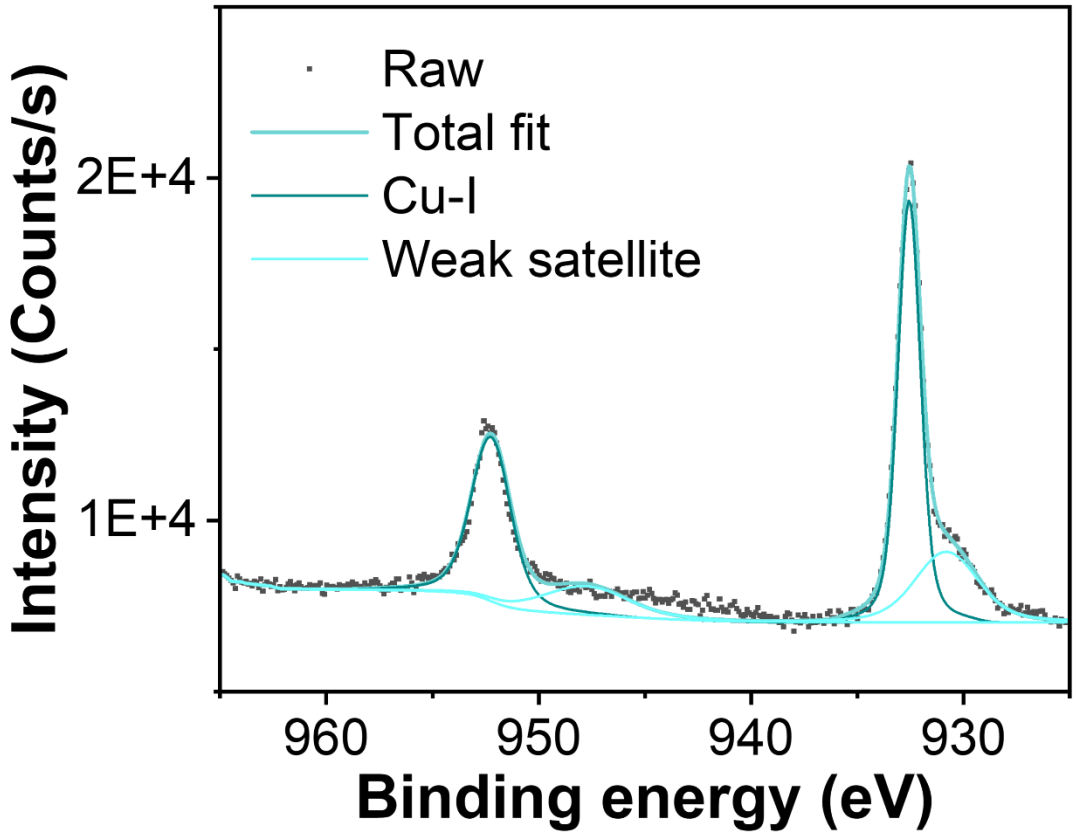

Fig. S23. XPS Cu2p core level spectrum of a CuI(*Hda*) thin film.

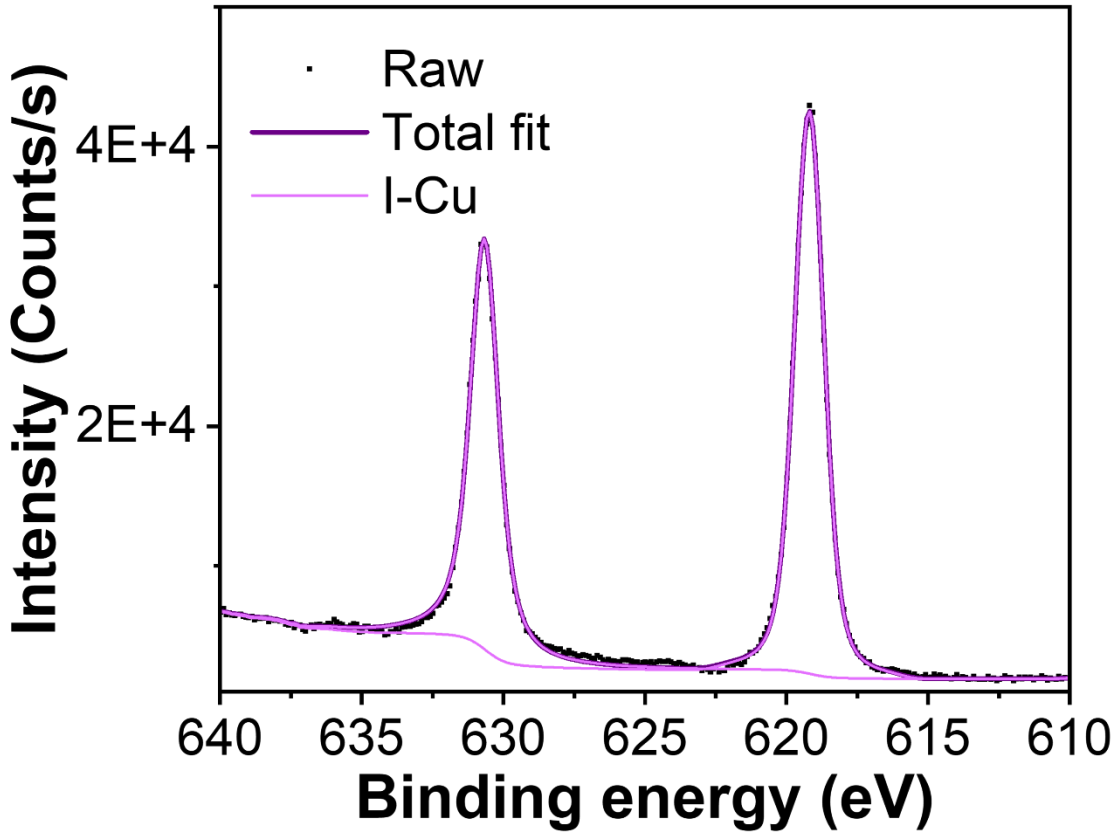

Fig. S24. XPS I3d core level spectrum of a CuI(*Hda*) thin film.

Table S6. Composition of the as-made CuI(*Hda*) thin film sample determined from XPS experiment compared to that calculated based on single crystal structure.

Elements	Expected (%)	Measured (%)
C	12	13.9
N	4	4
O	0	0.3
Cu	2	2.4
I	4	5.4

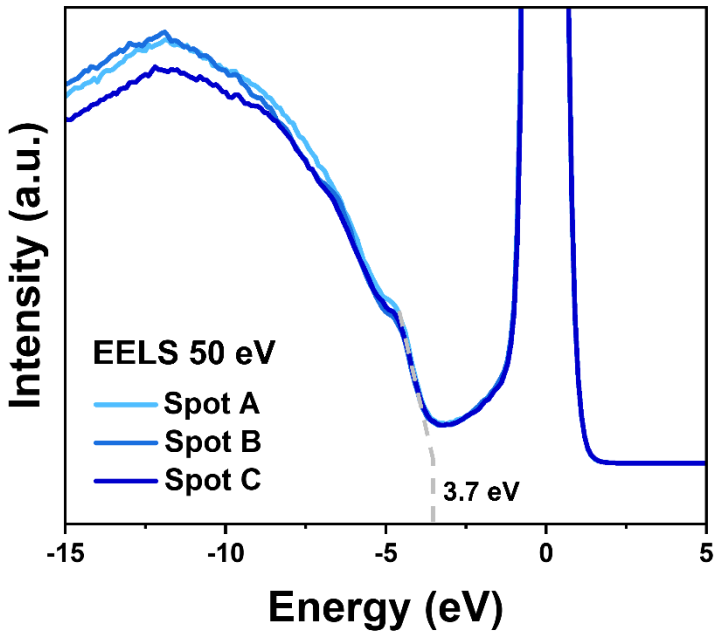

Fig. S25. REELS spectrum measured on the CuI(*Hda*) thin film.

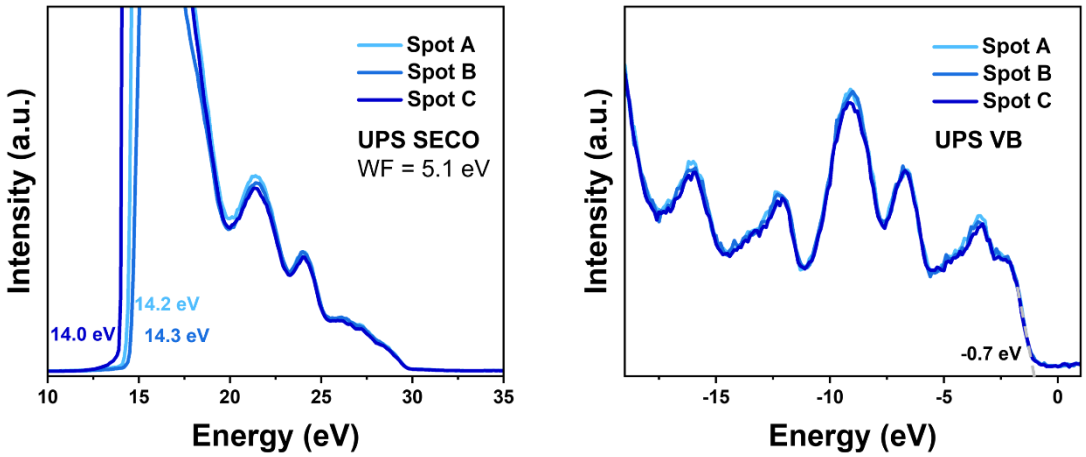

Fig. S26. Secondary electron cutoff (SECO) and valence band (VB) of the CuI(*Hda*) thin film measured in UPS.

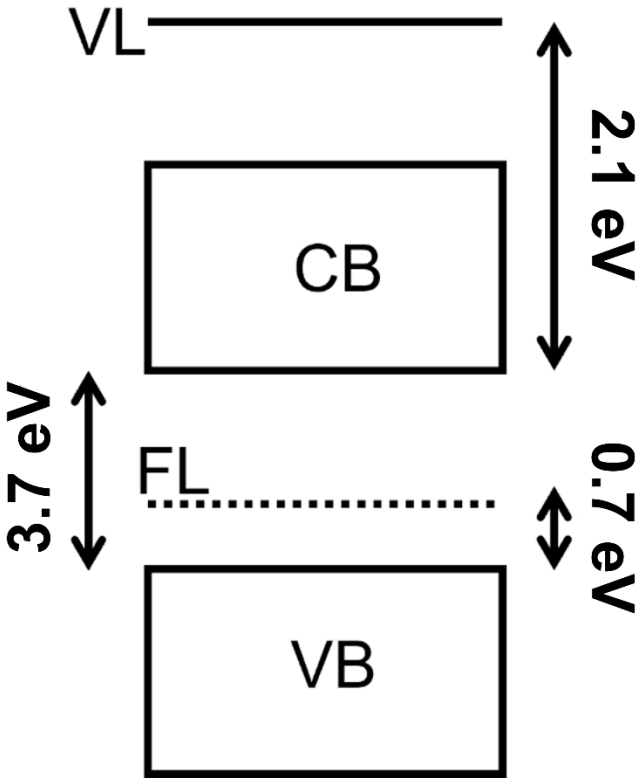

Fig. S27. Summarized energy diagram of CuI(*Hda*) determined from photoemission experiments.

Supplementary note 4. Synthesis and characterization of 2PACz-based SAM materials
The NMR spectra were obtained at 25 °C with a Bruker Avance Neo 500 MHz. Chemical shifts are given in ppm relative to TMS, calibrated with either the TMS peak or the known chemical shifts of DMSO-d_6. ESI MS was obtained on a Waters Xevo G2-XS QTof Instrument.

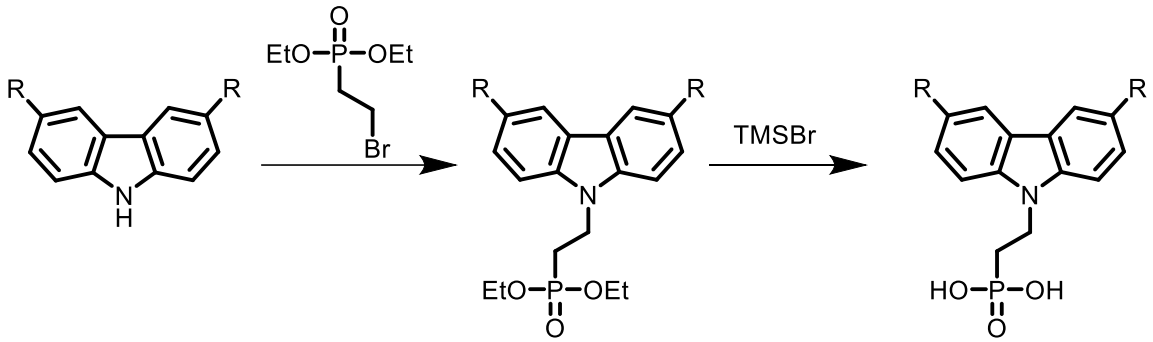

1a, R = H
1b, R = Br
1c, R = OMe
1d, R = Ac

2a, R = H
2b, R = Br
2c, R = OMe
2d, R = Ac

3a (2PACz), R = H
3b (Br2PACz), R = Br
3c (MeO2PACz), R = OMe
3d (Ac2PACz), R = Ac

Substituted carbazole compounds **1b**, **1c** and **1d** were synthesized and purified by reported methods[1-3].

General procedure for **3a**-**3d**[4]:
To **1** (11.13 mmol) in dry DMSO (20 mL) NaH (0.49 g, 12.24 mmol) was added, and the solution was stirred for 0.5 h at room temperature under N_2. Then, diethyl (2-bromoethyl)phosphonate (2.64 g, 12.24 mmol) was added and the mixture was heated at 60 °C for 20 h. The reaction mixture was poured into water (100 mL), acidified with 1 M hydrochloric acid and then extracted with ethyl acetate (3 × 100 mL). The combined organic extracts were washed with brine, dried with magnesium sulfate and the solvent was removed. The residue was dissolved in a minimum amount of ethyl acetate and chromatographic separation on silica was achieved to give **2**. To **2** (10 mmol) in dry CH_2Cl_2 (20 mL) trimethylsilyl bromide (2.90 mL, 22 mmol) was added under N_2. The solution was stirred for 6 h before being quenched with MeOH and stirred vigorously. After a further 2 h stirring the solvent was removed under reduced pressure and water (5 mL) was added. The mixture was then concentrated under reduced pressure. This step was repeated four times to give **3**.

Characterization data of **3a**-**3d**:

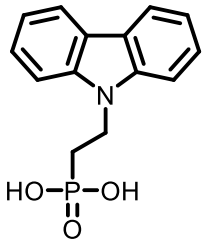

3a

^{1}H NMR (500 MHz, DMSO-d_6) δ 8.16-8.15 (m, 2H), 7.55-7.46 (m, 4H), 7.23-7.20 (m, 2H), 4.57-4.56 (m, 2H), 2.07- 2.00 (m, 2H).
^{13}C NMR (126 MHz, DMSO-d_6) δ 139.43, 125.89, 122.32, 120.44, 119.00, 108.96, 37.39, 27.83.
ESI-MS-Negative calcd for $C_{14}H_{13}NO_3P$ $[M-H]^-$ 274.0711, found 274.0990.

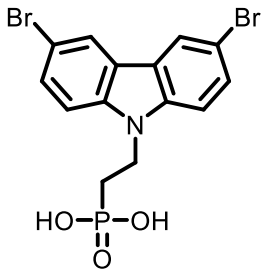

3b

^{1}H NMR (500 MHz, DMSO-d_6) δ 8.47-8.46 (m, 2H), 7.64-7.61 (m, 2H), 7.55-7.54 (m, 2H), 4.56-4.51 (m, 2H), 2.06-1.99 (m, 2H).
^{13}C NMR (126 MHz, DMSO-d_6) δ 138.59, 128.97, 123.53, 123.18, 111.52, 111.44, 37.77, 27.67.
ESI-MS-Negative calcd for $C_{14}H_{11}Br_2NO_3P$ $[M-H]^-$ 429.8922, found 429.9305.

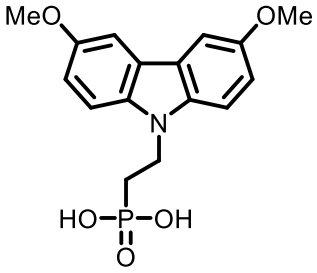

3c

^{1}H NMR (500 MHz, DMSO-d_6) δ 7.73 (d, J = 2.5 Hz, 2H), 7.39 (d, J = 8.8 Hz, 2H), 7.07 (dd, J = 8.8, 2.5 Hz, 2H), 4.46 (m, 2H), 3.85 (s, 6H), 1.95 (m, 2H).
^{13}C NMR (126 MHz, DMSO-d_6) δ 153.05, 134.96, 122.65, 115.00, 109.74, 103.44, 55.70, 37.54, 27.94, 26.90.
ESI-MS-Negative calcd for $C_{16}H_{17}NO_5P$ $[M-H]^-$ 334.0923, found 334.1367.

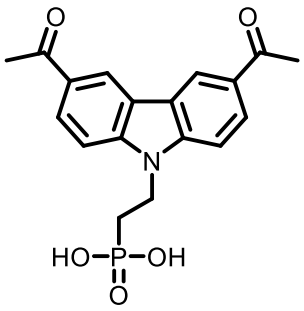

3d

^{1}H NMR (500 MHz, DMSO-d_6) δ 9.04 (d, J = 1.5 Hz, 2H), 8.13 (dd, J = 8.7, 1.7 Hz, 2H), 7.69 (d, J = 8.7 Hz, 2H), 4.63 (m, 2H), 2.70 (s, 6H), 2.09 (m, 2H).
^{13}C NMR (126 MHz, DMSO-d_6) δ 197.10, 142.94, 129.46, 126.59, 122.62, 122.45, 109.54, 38.00, 27.76, 26.77.
ESI-MS-Negative calcd for $C_{18}H_{17}NO_5P$ $[M-H]^-$ 358.0923, found 358.1132.

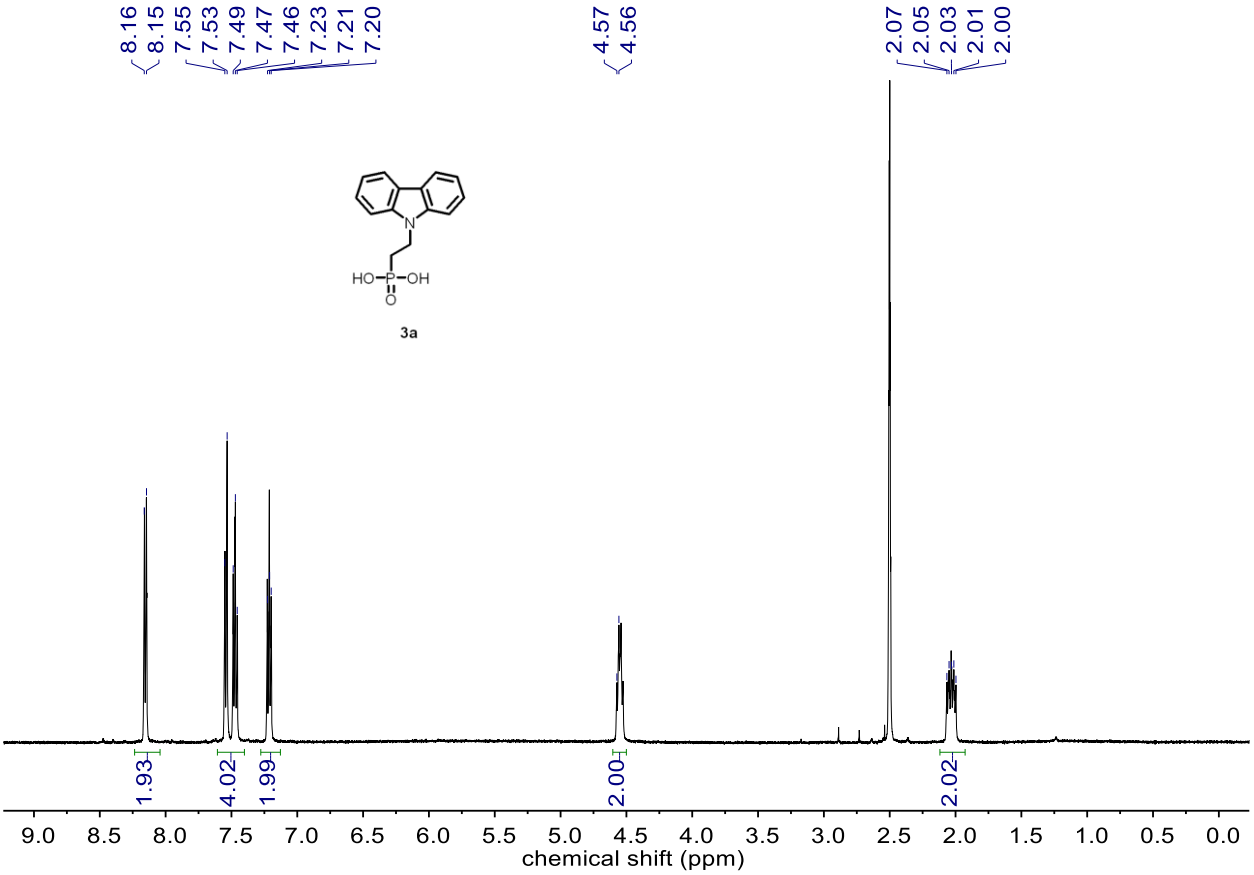

Fig. S28. ^{1}H NMR spectrum of **3a** (2PACz).

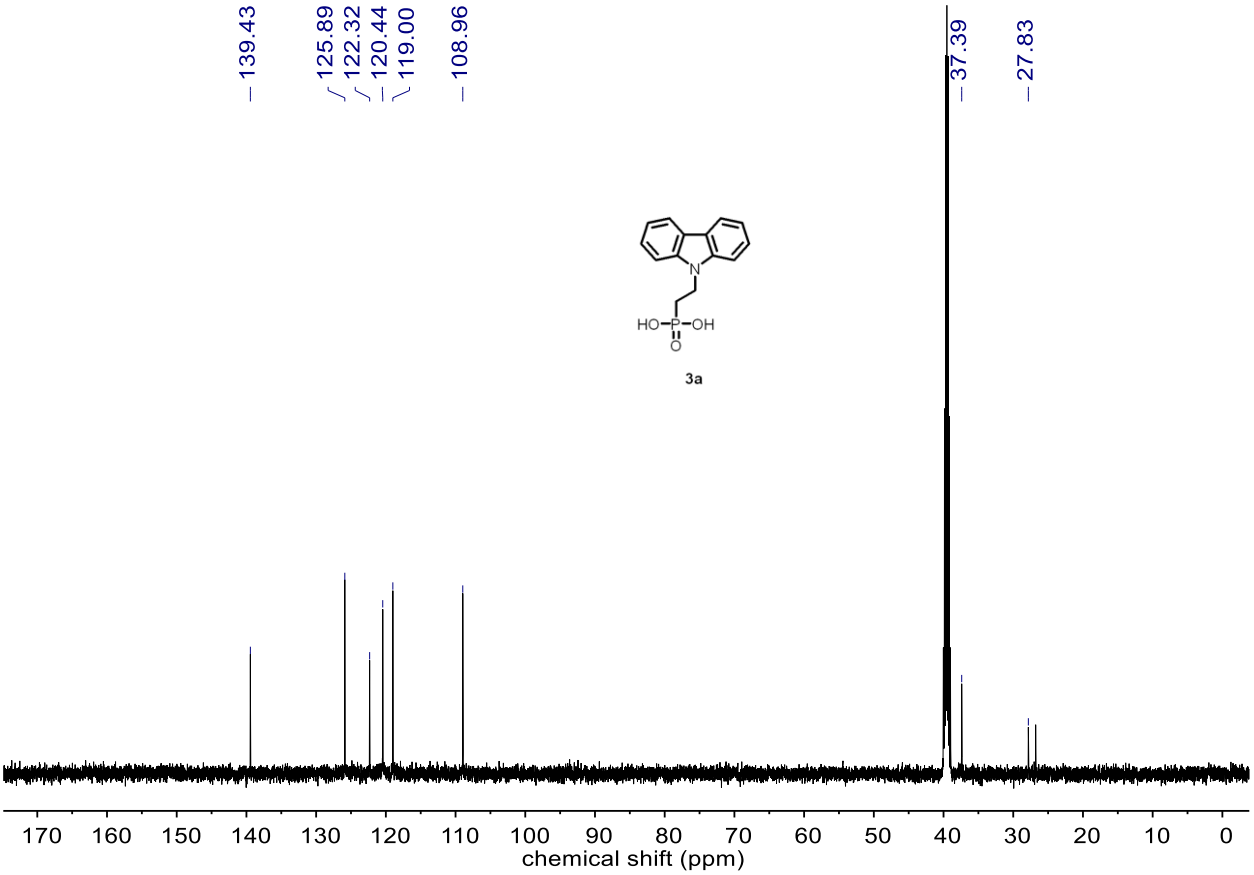

Fig. S29. ^{13}C NMR spectrum of **3a** (2PACz).

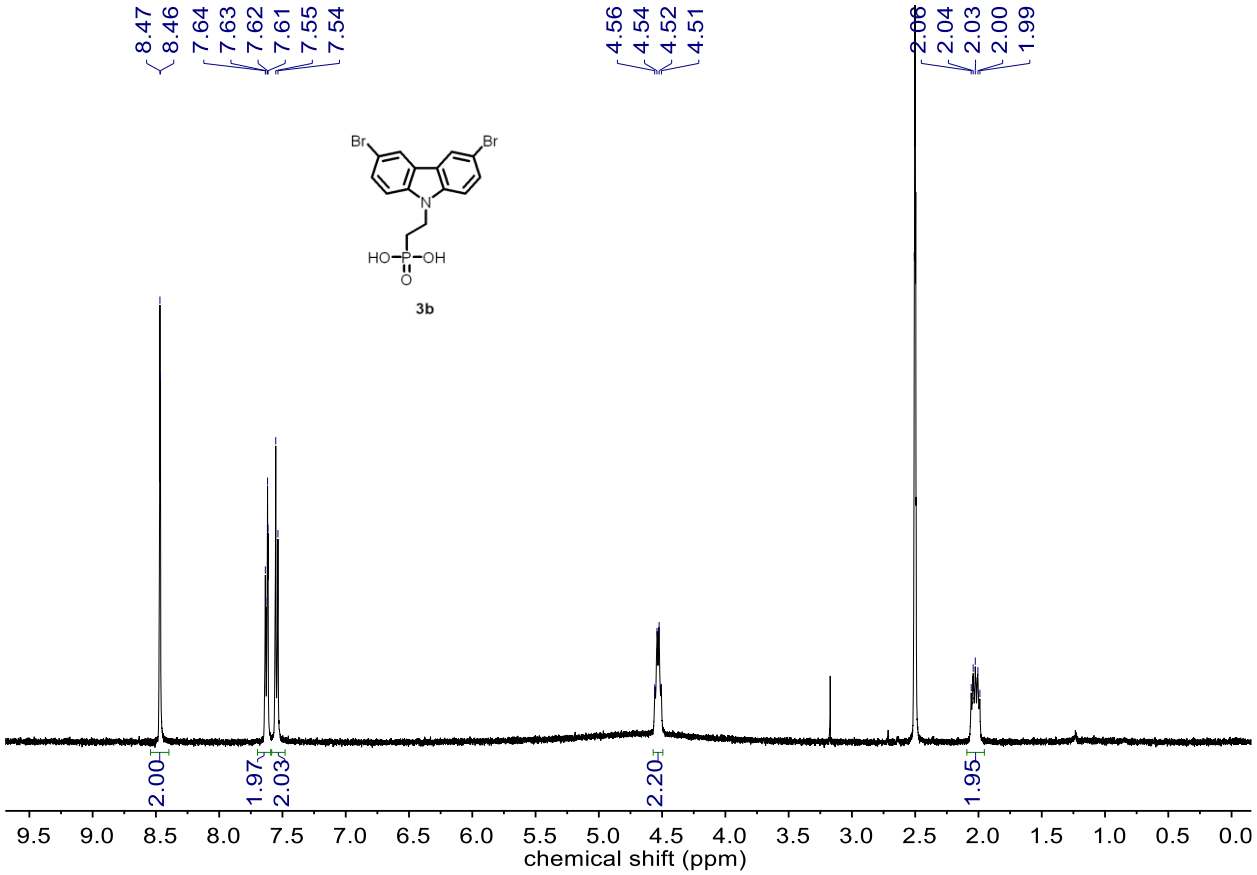

Fig. S30. ^{1}H NMR spectrum of **3b** (Br2PACz).

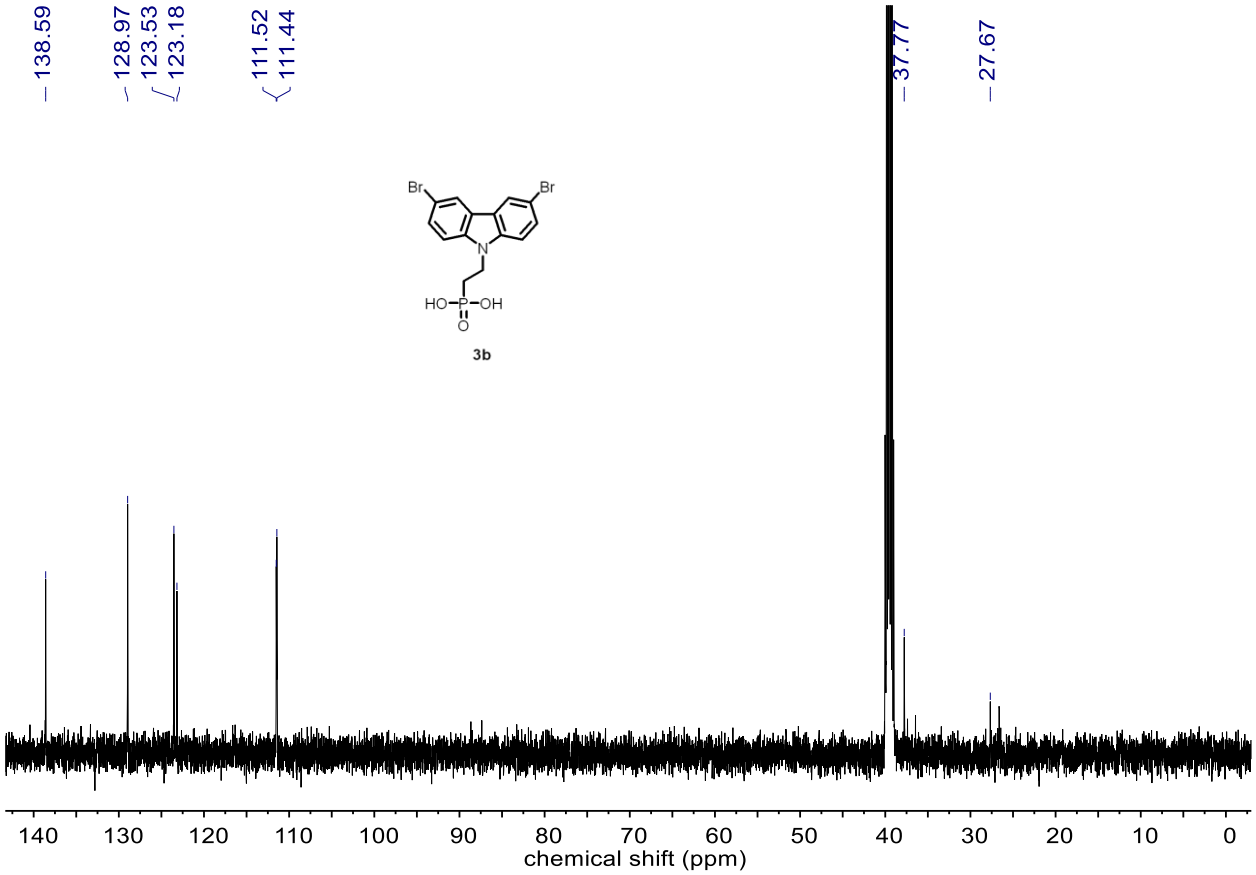

Fig. S31. ^{13}C NMR spectrum of **3b** (Br2PACz).

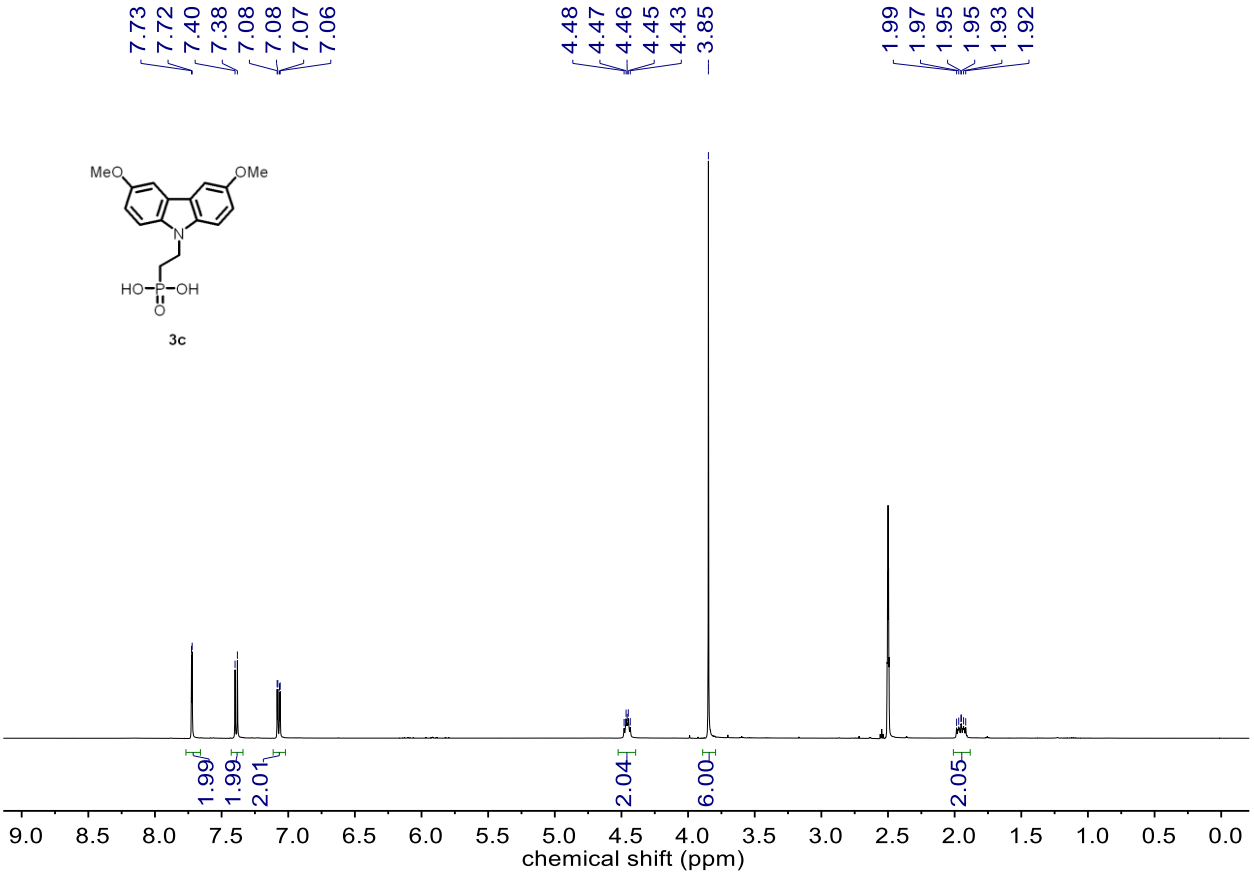

Fig. S32. ^{1}H NMR spectrum of **3c** (MeO2PACz).

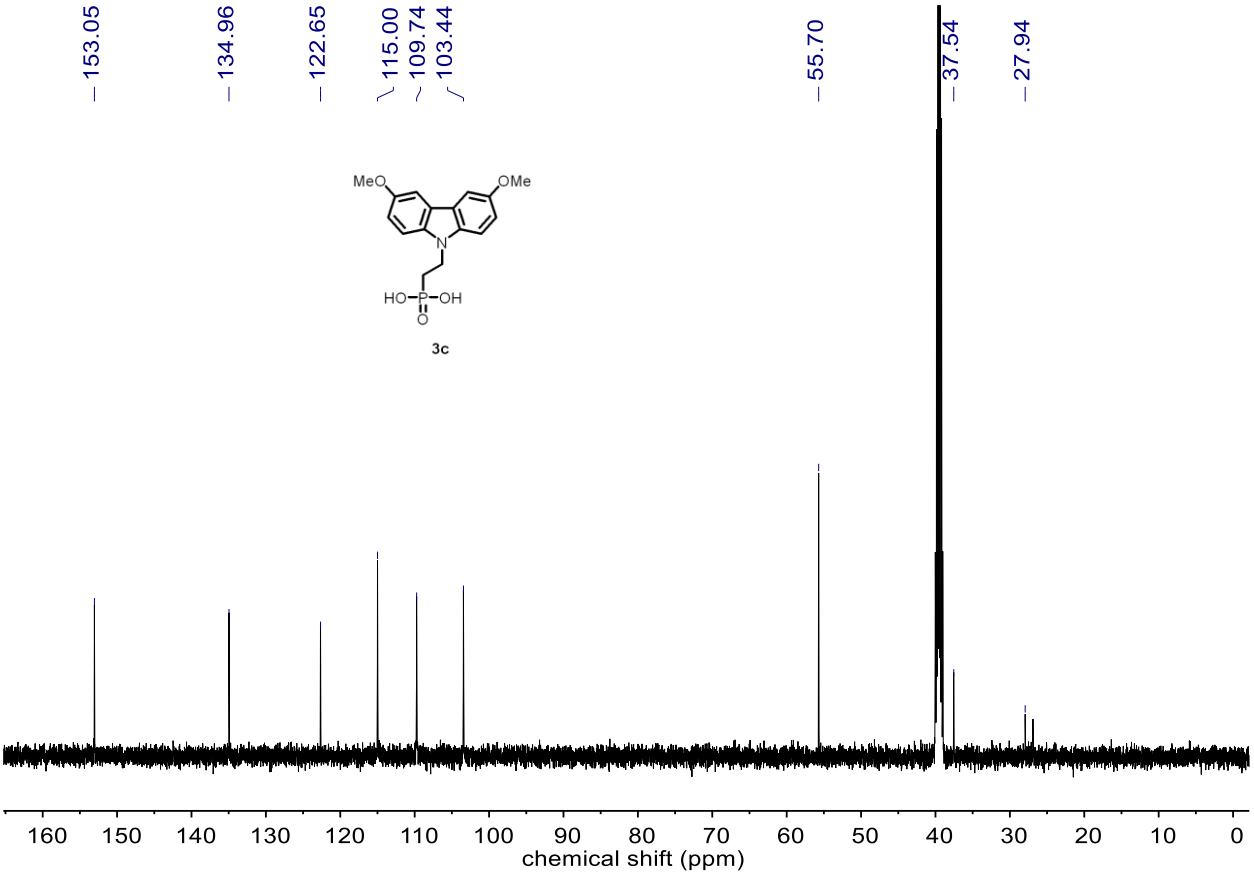

Fig. S33. ^{13}C NMR spectrum of **3c** (MeO2PACz).

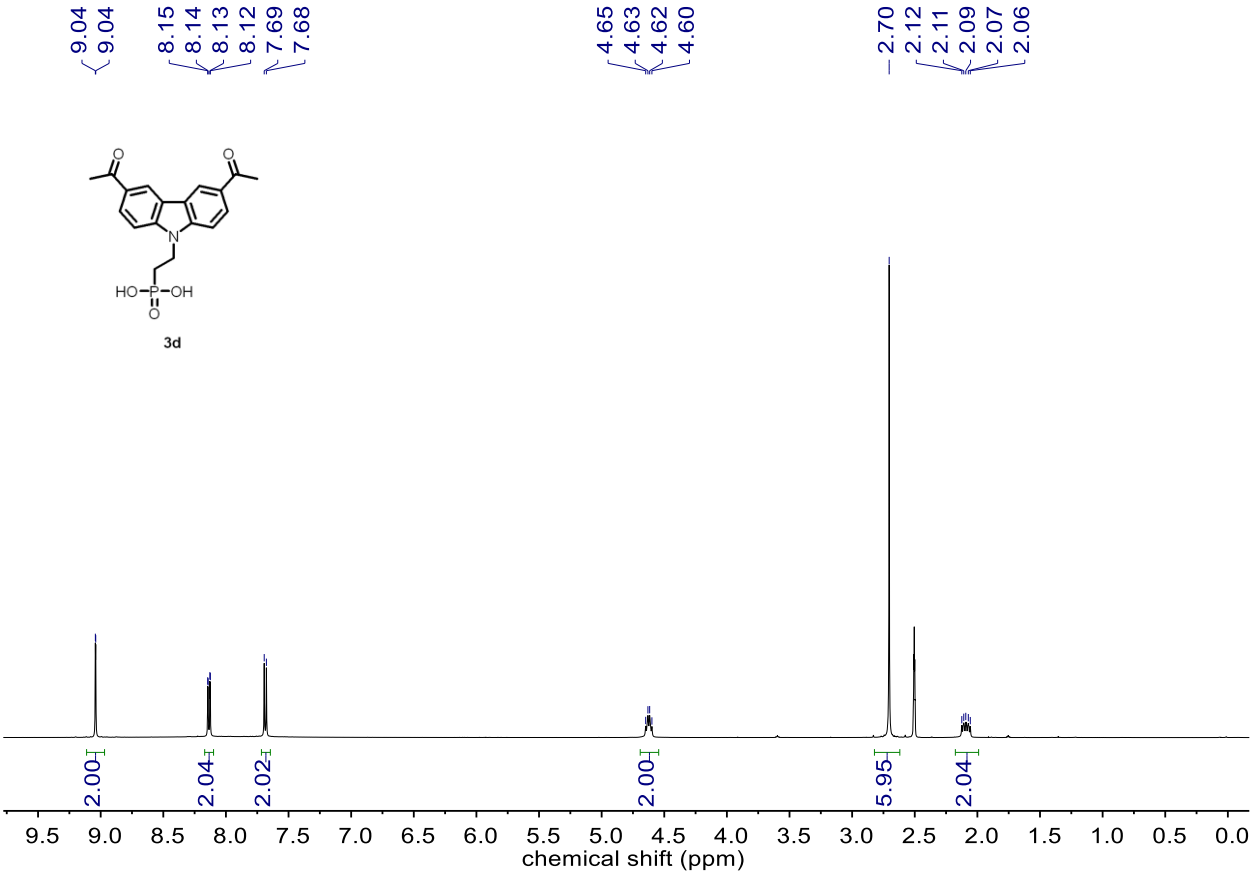

Fig. S34. ^{1}H NMR spectrum of **3d** (Ac2PACz).

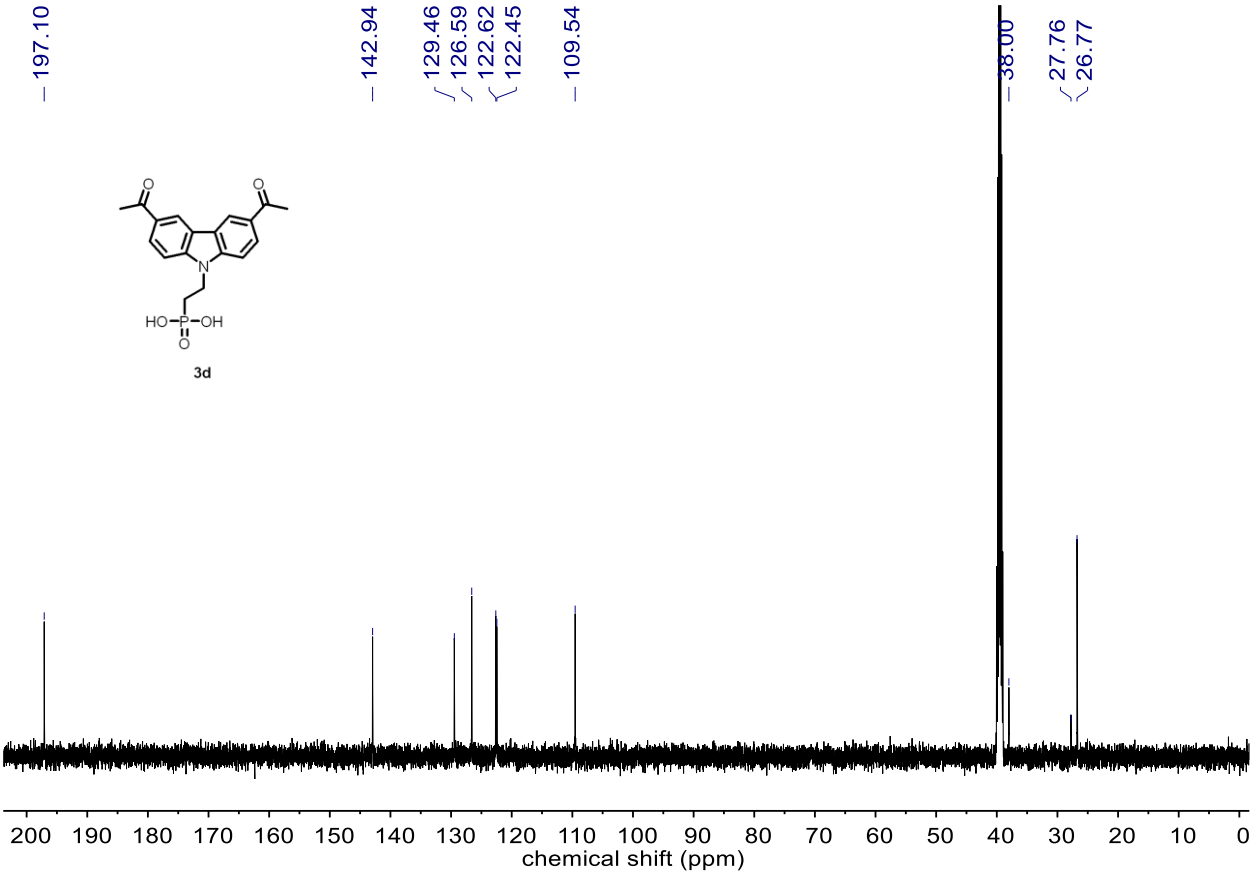

Fig. S35. ^{13}C NMR spectrum of **3d** (Ac2PACz).

Ellipsometry characteristics of sputtered NiO_x HTL

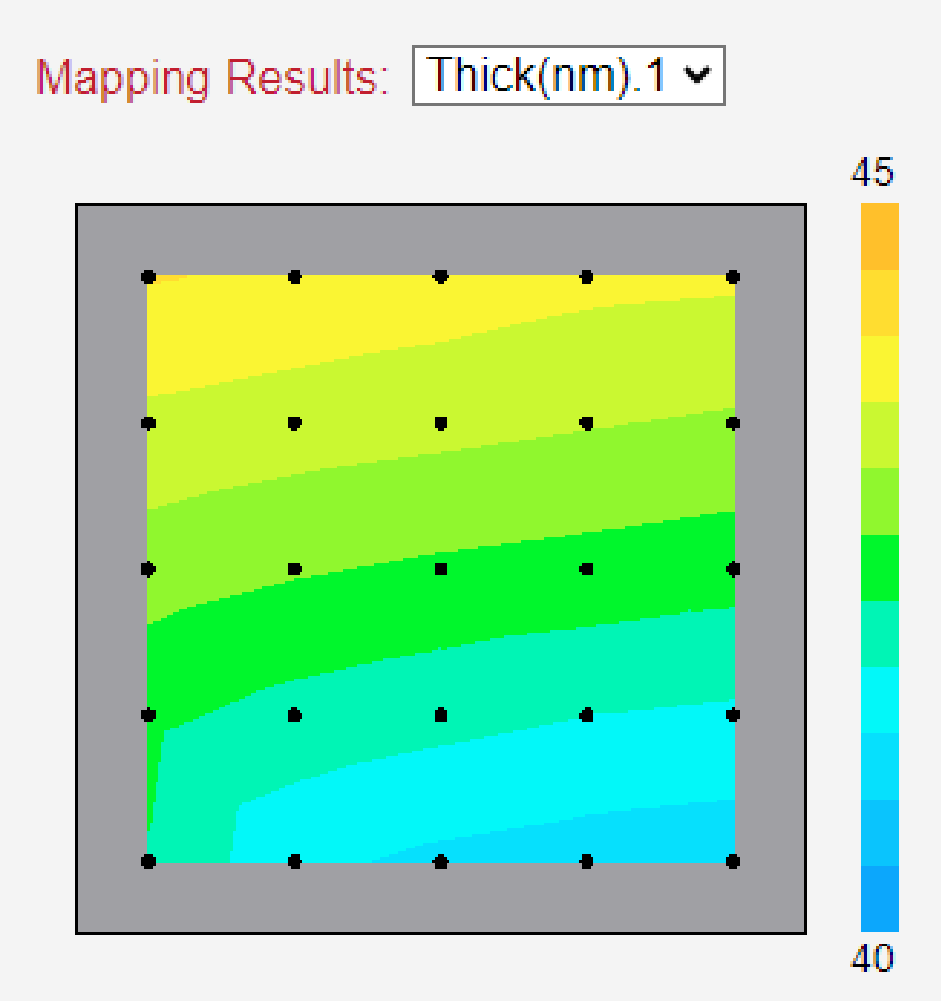

Fig. S36. Thickness mapping of a sputtered NiO_x thin film on ITO by ellipsometry.

Surface adsorption of SAMs on NiO (111)

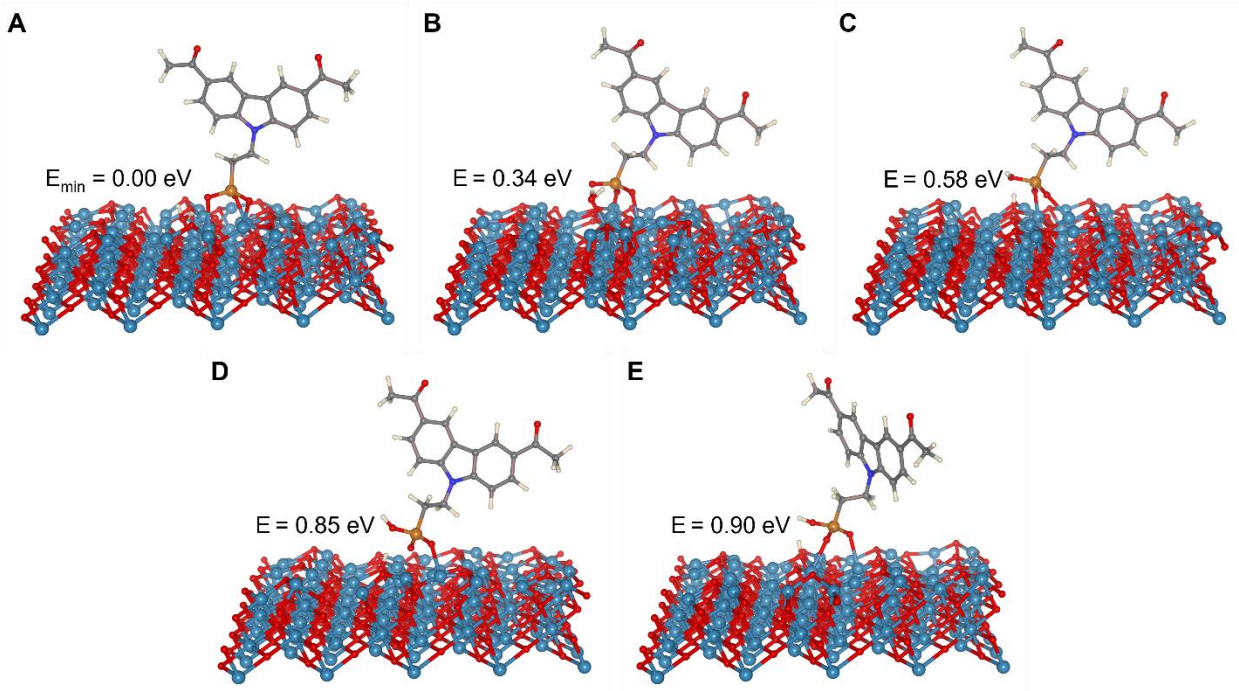

Fig. S37. Different adsorption configurations for SAMs of Ac2PACz molecules on the bare (111) surface of NiO. The values give the energy of each structure referenced to the energy of the most stable one (A). For the latter configuration (A), the chemisorption energy with respect to an Ac2PACz molecule in a vacuum is about 2.57 eV.

XPS of SAMs functionalized NiO_x

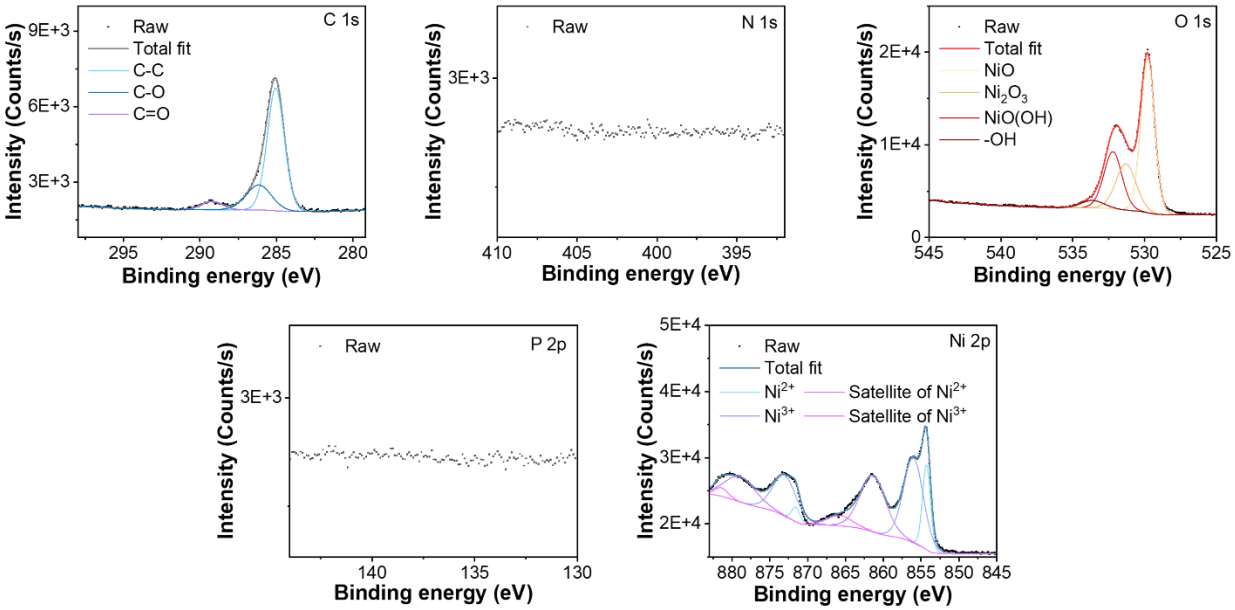

Fig. S38. XPS core level spectra of bare NiO_x thin film.

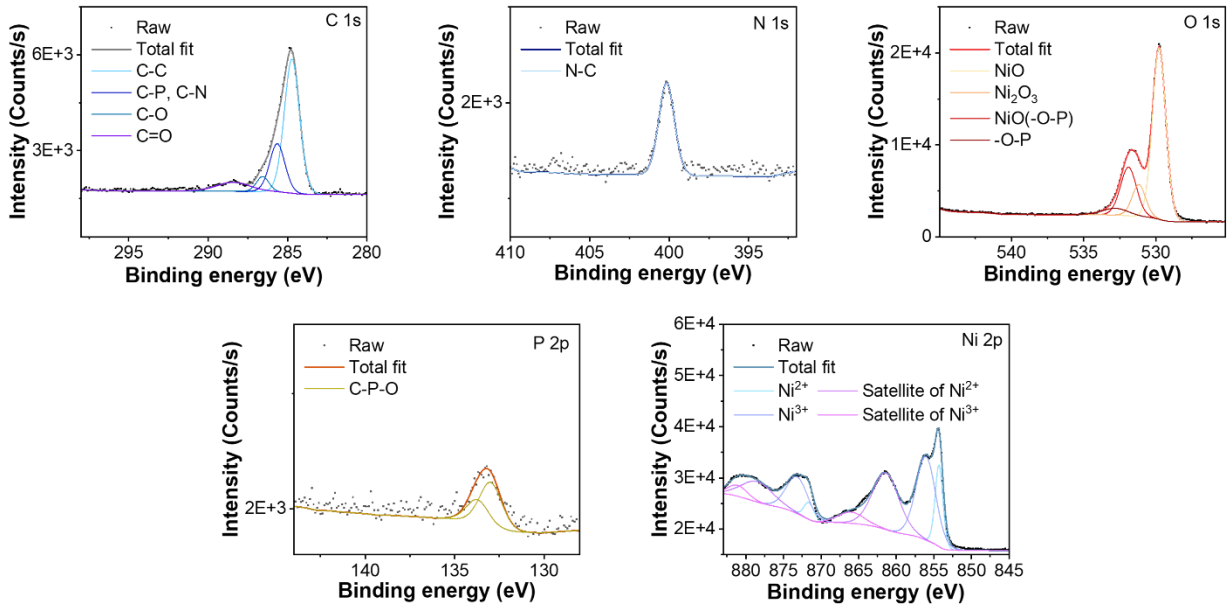

Fig. S39. XPS core level spectra of 2PACz-NiO_x thin film.

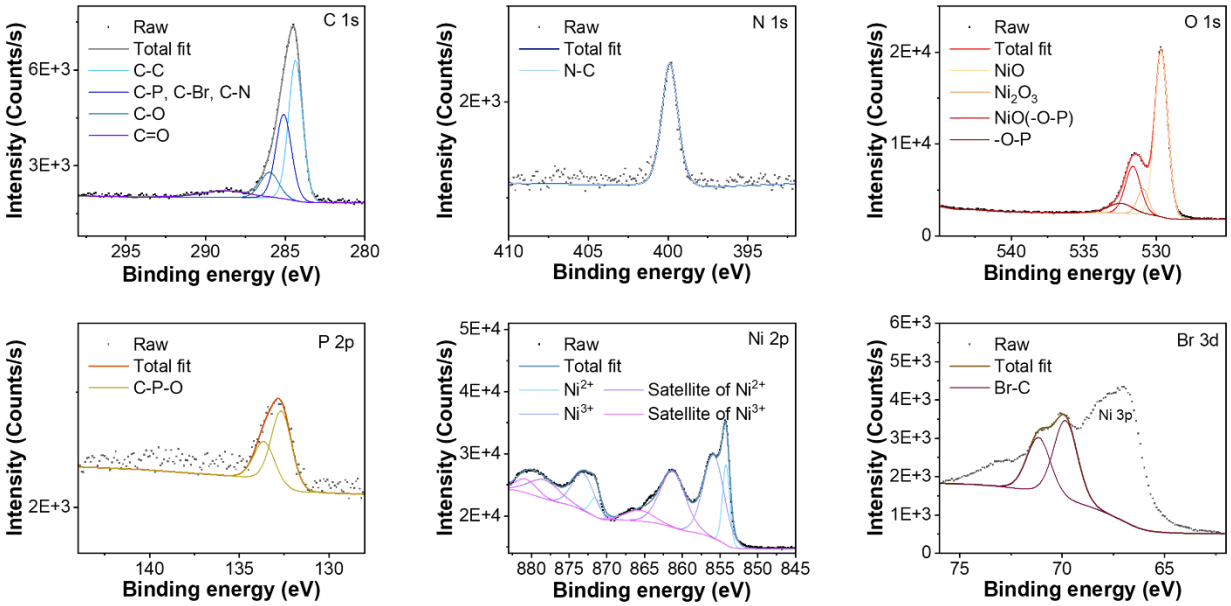

Fig. S40. XPS core level spectra of Br2PACz-NiO_x thin film.

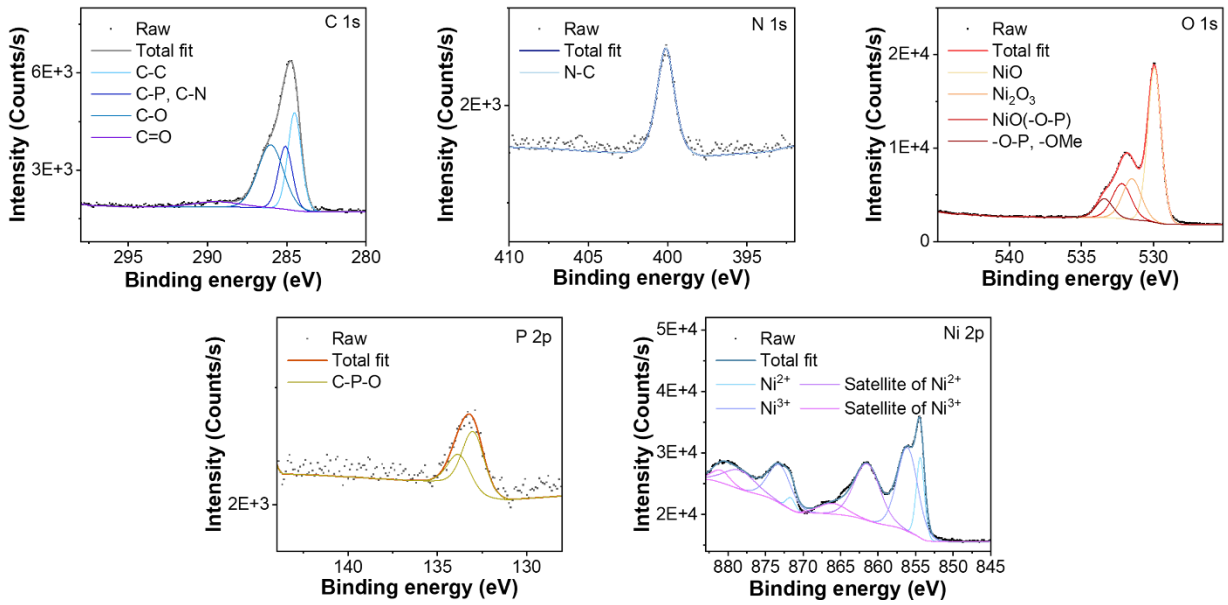

Fig. S41. XPS core level spectra of MeO2PACz-NiO_x thin film.

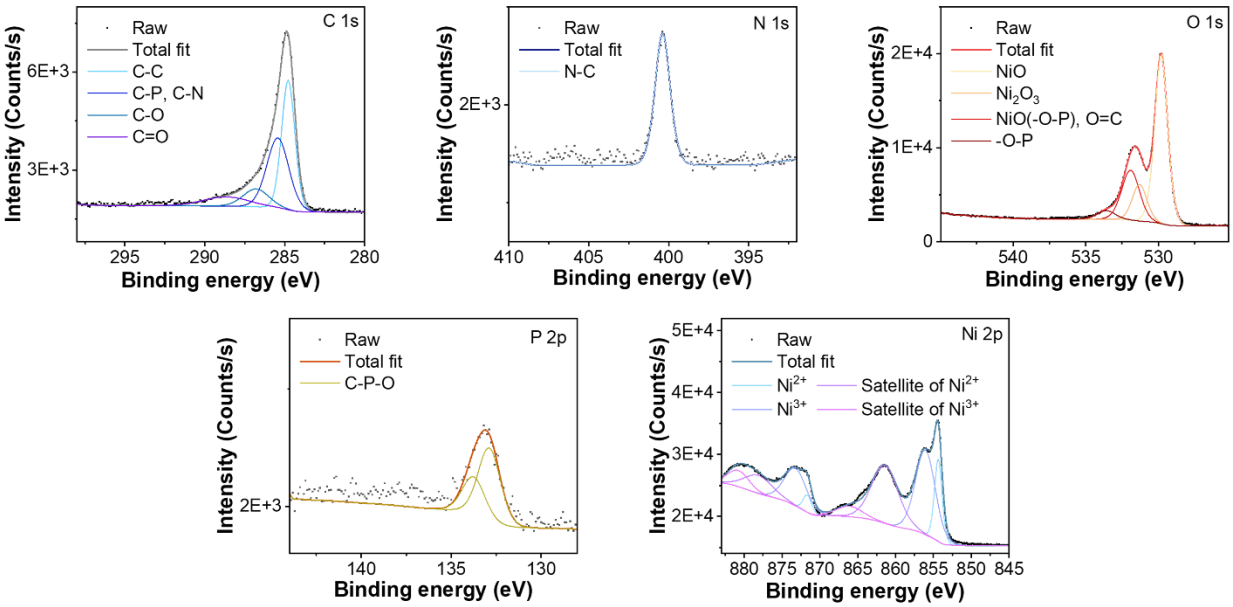

Fig. S42. XPS core level spectra of Ac2PACz-NiO_x thin film.

Supplementary note 5. Angular resolved XPS (AR-XPS) for coverage determination of the Ac2PACz SAM on NiO_x

The SAM coverage on the can be quantified and determined from the AR-XPS over-layer signal of the surface layer to that of the NiO_x thin film[5,6]. Here the integrated intensity of the P $2p_{3/2}$ peak of the Ac2PACz, and the Ni^{2+} $2p_{3/2}$ peak are used, as shown in Figure 4C for the photoelectron emission angles (0-75°). The XPS ratio expected for an ideal complete or partial monolayer of molecules can first be calculated. The relative sensitivity factor (SF) for P $2p_{3/2}$ and Ni $2p_{3/2}$ is 0.0632 using the adapted Casa XPS library. Furthermore, the instrumental transmission function (TXFN) specific to the K-alpha spectrometer and lens apertures was adapted. The emission of photoelectrons from a surface has a finite depth resulting from inelastic and elastic attenuation processes. This can be represented by the attenuation length λ, which is the thickness at which the intensity reduces to 1/e at normal angle 0° and the attenuated intensity is described by the Equation S5.

$$I = I_0 e^{\left(-\frac{d}{\lambda\, cos(\theta)}\right)} \tag{S5}$$

where I is the attenuated intensity, I_0 the non-attenuated intensity, d the depth from which they originate and θ the angle with respect to normal.

To determine λ for NiO_x, a simplified universal attenuation length formula[7] is used for and is given as Equation S6:

$$\frac{\lambda}{a} = (1.861 + 0.00132Z^{1.7} + 0.0282E^{0.93})/Z^{0.38} \tag{S6}$$

where a is the layer thickness in nm and Z is the average atomic number of NiO_x and E is the photoelectron kinetic energy of the core level analyzed, here for the Ni $2p_{3/2}$ an λ of 1.4 nm is calculated.

For the Ac2PACz, an organic universal formula S7 is adapted:

$$\lambda = 0.00837E^{0.842} \tag{S7}$$

in nm for the SAM of Ac2PACz 2.46 nm (Ni $2p_{3/2}$) and overlayer of functionalized carbazole group 3.61 nm (P $2p_{3/2}$) are used.

Considering a crystalline surface of NiO (111), the Ac2PACz molecule occupies approximately 0.23 nm^2 area as used for phosphonic acid, which is in close agreement with an earlier QCM (quartz microbalance) study[8] of PA on SiO2/Si (0.18 nm^2) and therefore a full occupancy can be considered to be a maximum of 4.4×10^{14} $molecules cm^{-2}$. The ratio of Ni in the n underneath layers of each Ac2PACz molecule is (1/3n). If a depth of 3λ (Ni $2p_{3/2}$) (95% of intensity) is considered, which is 4.2 nm containing 17.43 layers of NiO monolayer, this leads to a factor of 1 P to 53.28 Ni atoms. Furthermore, the electrons from In and P are also attenuated by passing through the Ac2PACz layer (coordinated by the -PO3H), where the height of Ac2PACz is effectively ~1.1 nm for Ni electrons and ~0.86 nm for P electrons as inferred from the adsorption model of Ac2PACz, this correction factor can be expressed in Equation S8 below, reducing to the simple ratio of exponential functions at 1 ML:

$$Overlayer\ correction\ function = \frac{\Phi e^{\left(-\frac{dAcCz(0.86\ nm)}{\lambda_{P\ 2p3/2}\cos(\theta)}\right)}}{1-\Phi+\Phi e^{\left(-\frac{dAc2PACz(1.1\ nm)}{\lambda_{Ni\ 2p3/2}\cos(\theta)}\right)}} \tag{S8}$$

where Φ is the coverage. Therefore, the full expression for the XPS ratio versus electron emission angle is shown as Equation S9:

$$\frac{I_{P\ 2p3/2}}{I_{Ni\ 2p3/2}} = \frac{1}{53.28} \times \frac{SF_{P\ 2p3/2}}{SF_{Ni\ 2p3/2}} \times \frac{\Phi e^{\left(-\frac{dAcCz(0.86\ nm)}{\lambda_{P\ 2p3/2}\cos(\theta)}\right)}}{1-\Phi+\Phi e^{\left(-\frac{dAc2PACz(1.1\ nm)}{\lambda_{Ni\ 2p3/2}\cos(\theta)}\right)}} \quad \text{(S19)}$$

The model P $2p_{3/2}$/Ni $2p_{3/2}$ ratio could be depicted as a function of coverage for the different emission angles used. Overall, a relatively saturated average coverage of 0.87 $\pm$ 0.21 is determined, indicating a near monolayer of Ac2PACz assembled on NiO_x surface.

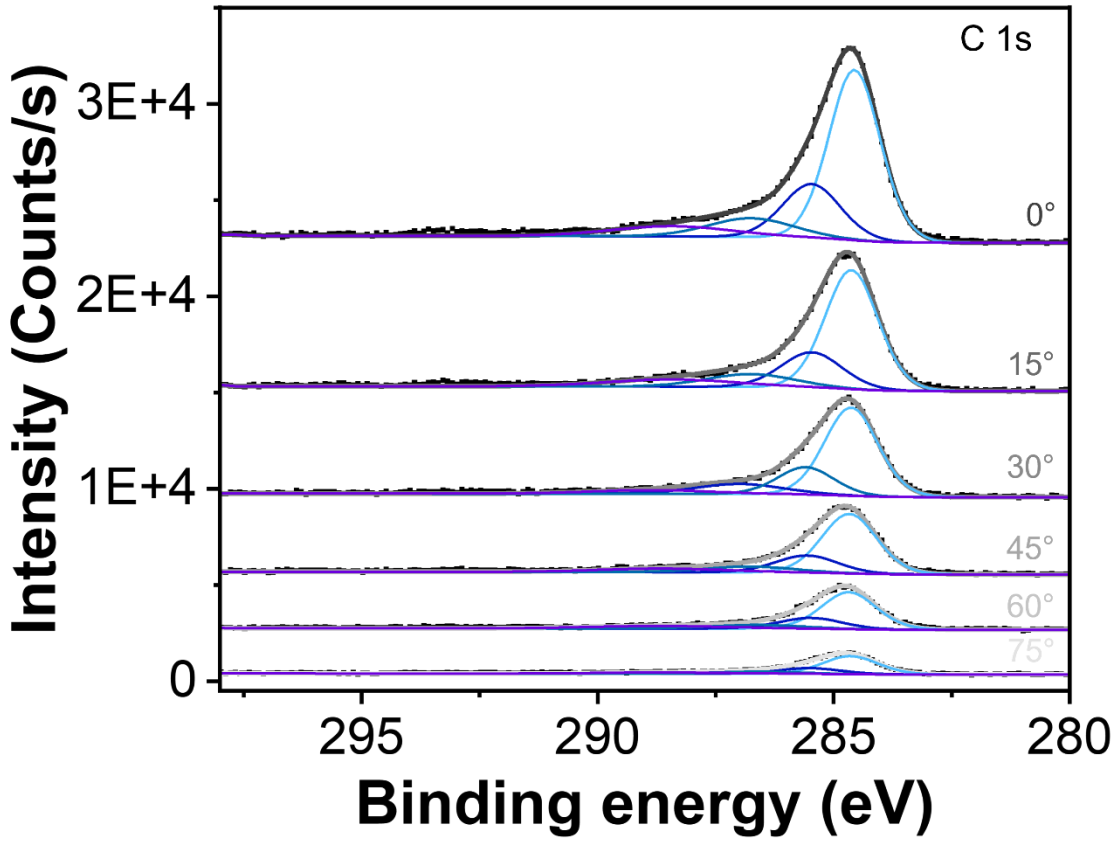

Fig. S43. ARXPS C1s spectra of a Ac2PACz-NiO_x thin film.

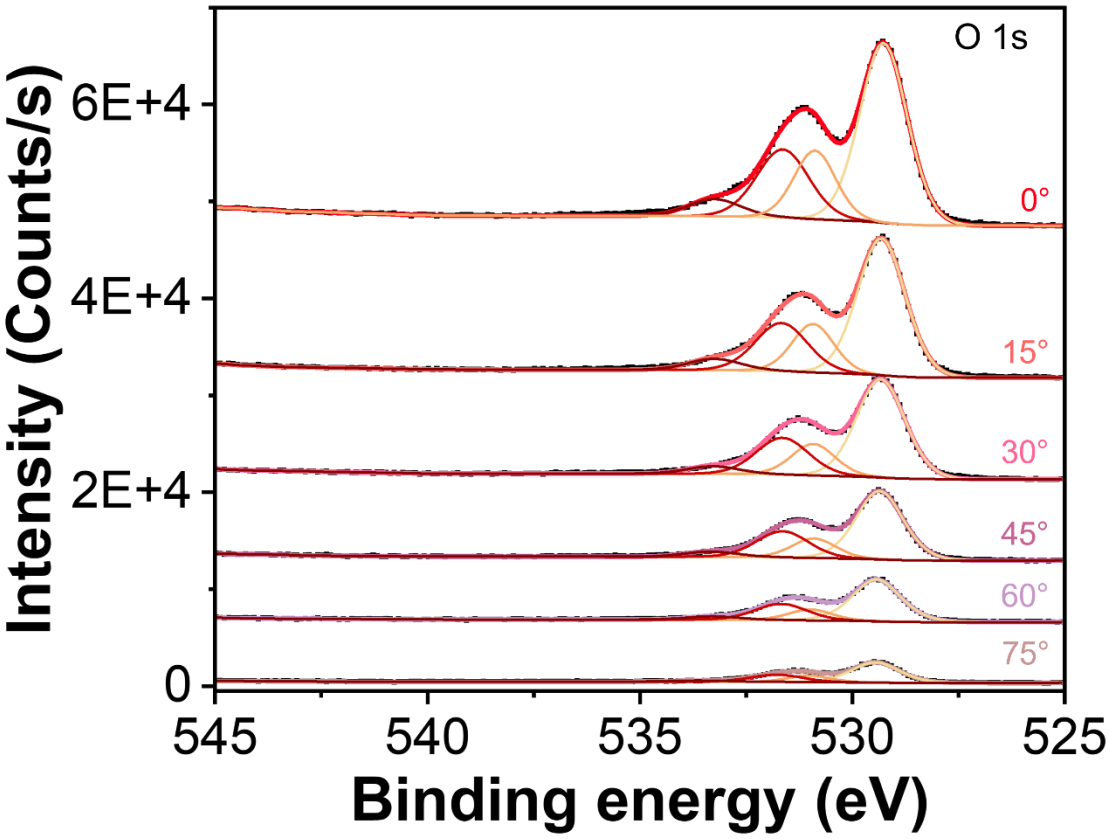

Fig. S44. ARXPS O1s spectra of a Ac2PACz-NiO_x thin film.

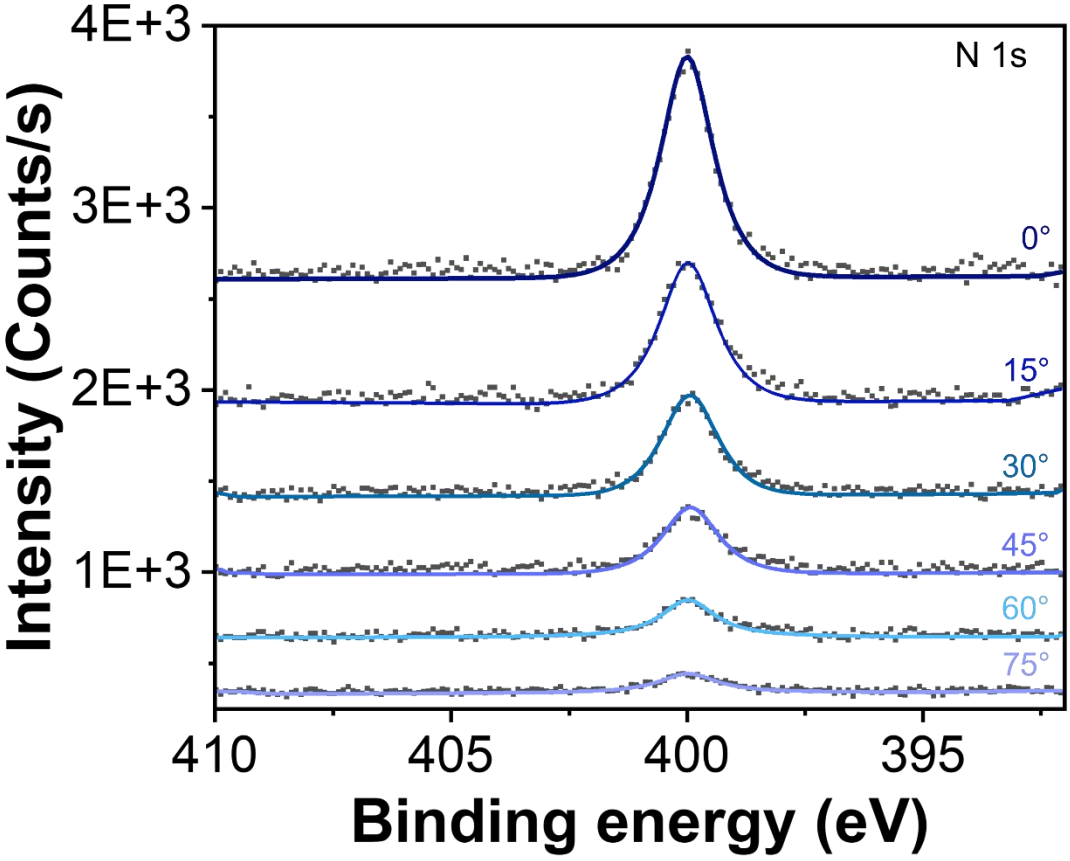

Fig. S45. ARXPS O1s spectra of a Ac2PACz-NiO_x thin film.

UV-vis absorption spectroscopy of 2PACz-based SAMs

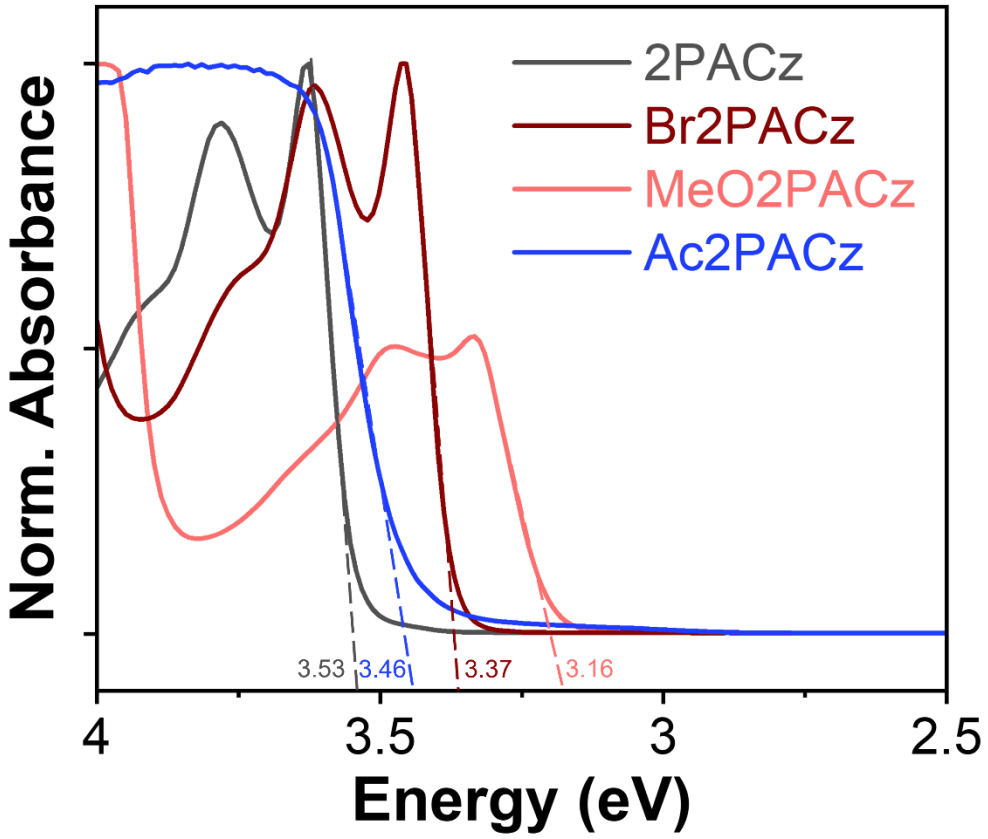

Fig. S46. UV-vis spectra of 2PACz-based SAMs.

Energy levels of 2PACz-based SAMs functionalized NiO_x

Table S7. Summary of VBM and CBM of 2PACz-based SAMs functionalized NiO_x HTLs.

HTL	VBM (eV)	CBM (eV)
Control NiO_x	-5.55	-1.60
2PACz-NiO_x	-5.70	-2.17
Br2PACz-NiO_x	-6.03	-2.66
MeO2PACz-NiO_x	-5.21	-2.05
Ac2PACz-NiO_x	-5.83	-2.37

Contact angle measurements of 2PACz-based SAMs functionalized NiO_x

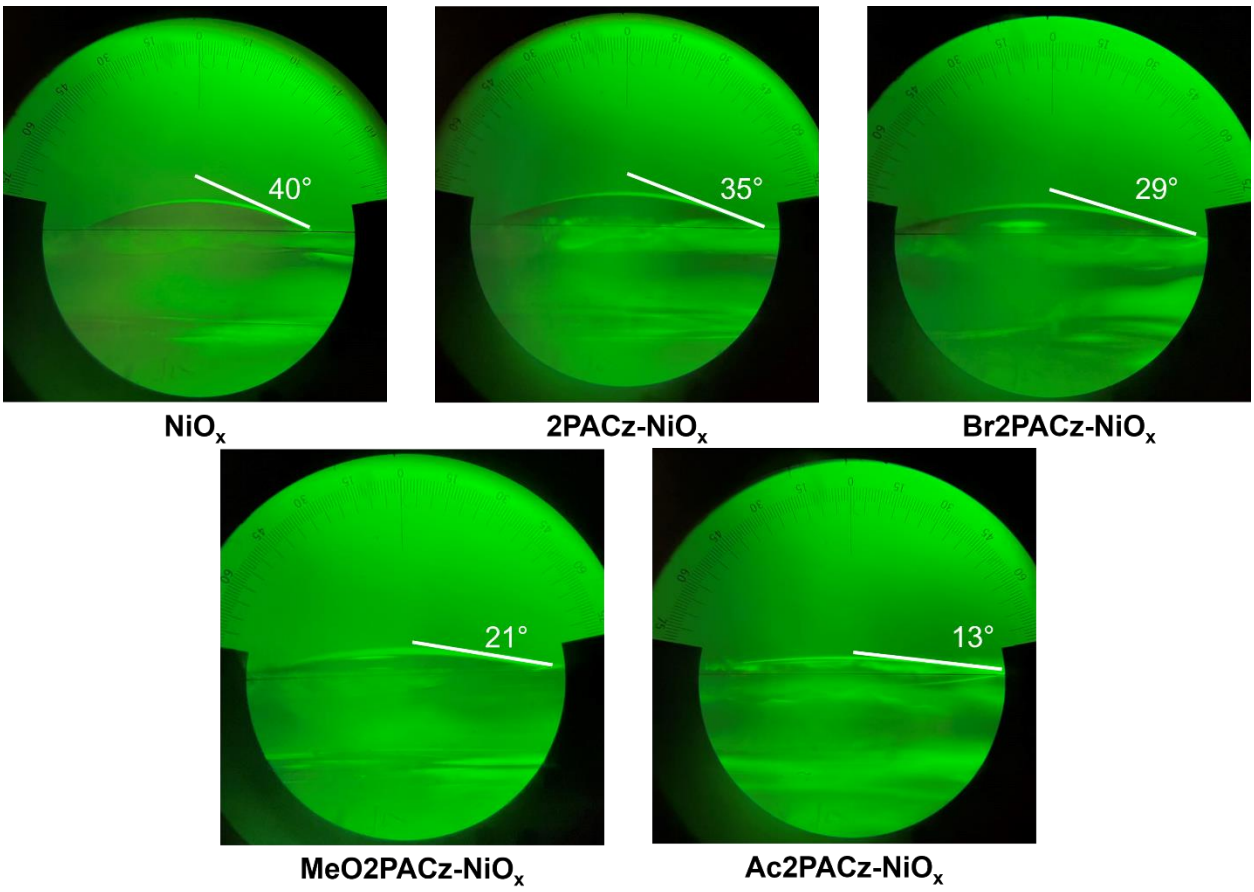

Fig. S47. Photographs of CuI(*Hda*)-DMF precursor droplets in contact with 2PACz-based SAMs functionalized NiO_x surfaces.

Supplementary note 6. Space charge-limited current (SCLC) measurements for hole-only devices with 2PACz-based SAMs functionalized NiO_x

Hole-only devices with 2PACz-based SAMs functionalized NiO_x as HTL was fabricated and compared. Decreased trap densities in all SAM-NiO_x were obtained, as the surface defect was highly passivated by the strong bonding between the phosphonic acid and NiO_x, while a stronger interaction between the substituted groups (-Ac>-OMe>-Br>-H) and the EML leads to a further decreasing in the V_{TFL}. Increased hole injection was achieved in 2PACz, Br2PACz and Ac2PACz, as the carbazole group was known as a favorable donor and a smaller barrier height on the HTL/EML heterojunction. The MeO2PACz showed poor hole injection as the energy alignment is unsuited, although a H-bond coupling on the interface was observed. In general, Ac2PACz outperformed the other SAMs, as a 1.5-fold hole mobility and a 3.6-times lower trap density was achieved on the H-bond coupled interface between HTL and EML, compared to the control NiO_x without SAM modification.

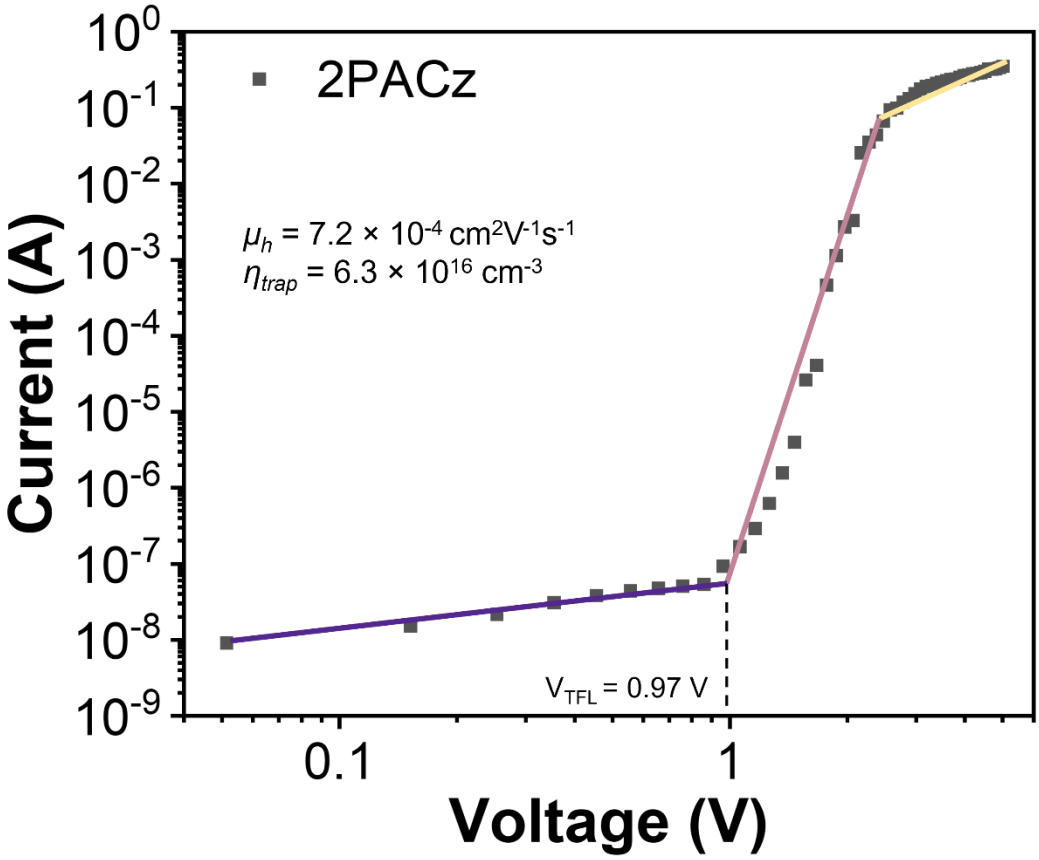

Fig. S48. SCLC measurements of an ITO/2PACz-NiO_x/CuI(*Hda*)/MoO_3/Au hole-only device.

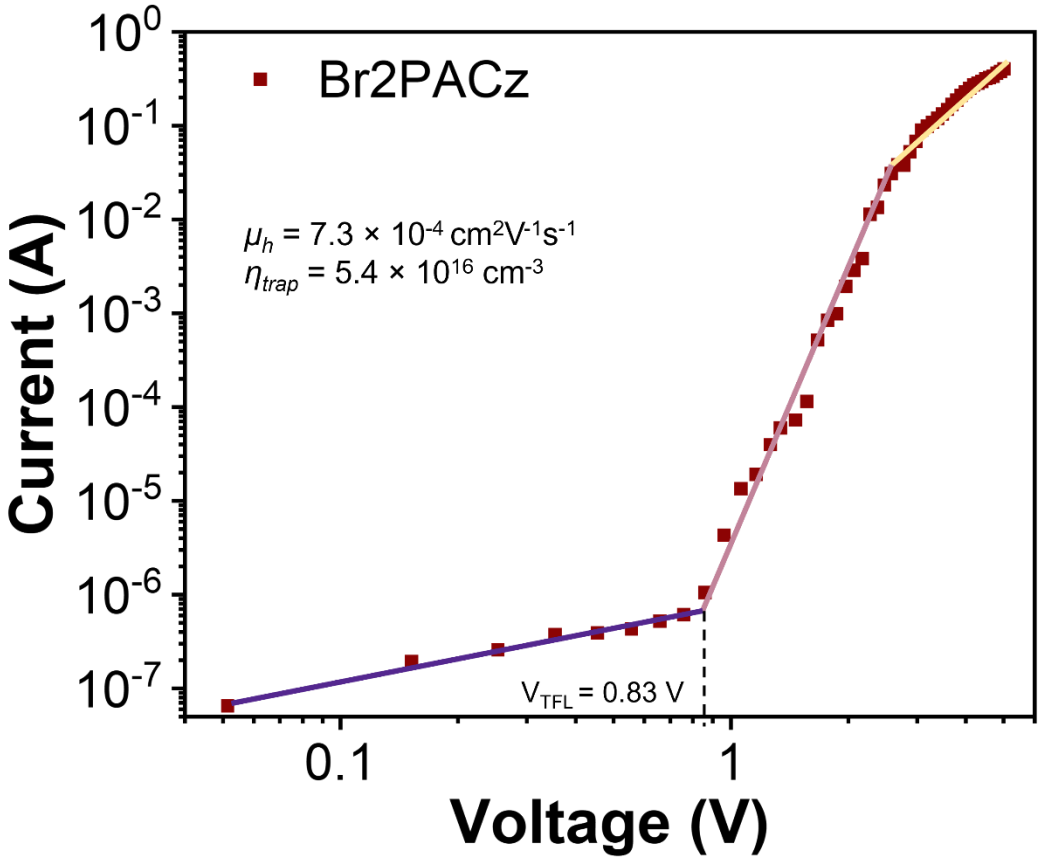

Fig. S49. SCLC measurements of an ITO/Br2PACz-NiO_x/CuI(*Hda*)/MoO_3/Au hole-only device.

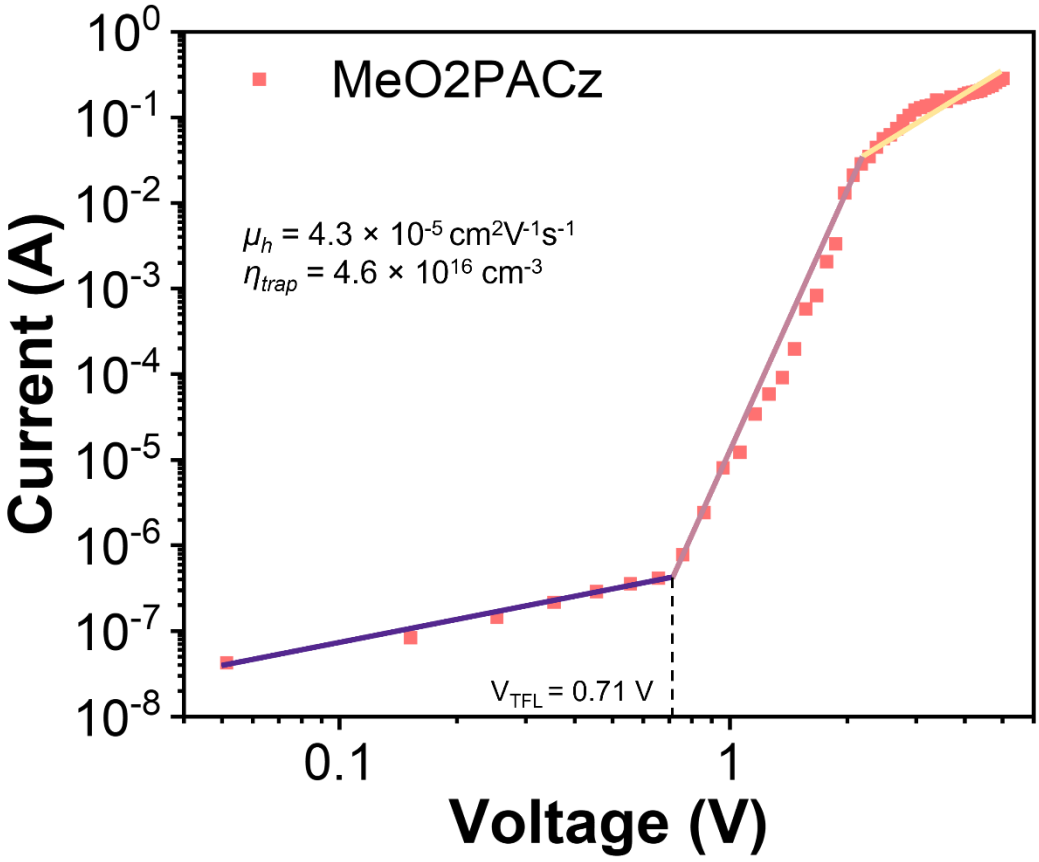

Fig. S50. SCLC measurements of an ITO/MeO2PACz-NiO_x/CuI(*Hda*)/MoO_3/Au hole-only device.

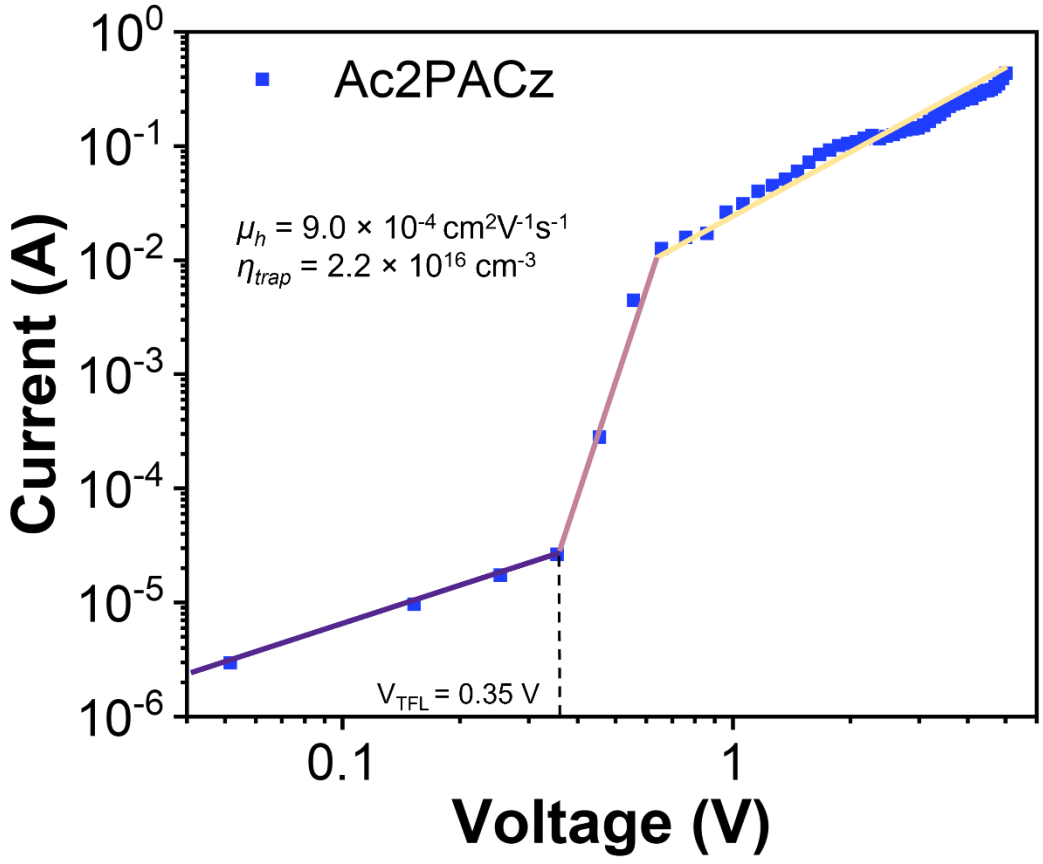

Fig. S51. SCLC measurements of an ITO/Ac2PACz-NiO_x/CuI(*Hda*)/MoO_3/Au hole-only device.

Supplementary note 7. ARXPS for thickness determination and H-bond interaction of the ultra-thin PMMA on CuI(*Hda*) EML

Thickness of ultra-thin PMMA overlayer with different spin-coating rate on EML is determined using ARXPS and similar algorism as SAM-NiO_x, while here the integrated intensity of the O 1s peak (Figure S55-57) of the PMMA [as the CuI(*Hda*) is nearly free of O in Fig. S25] and the I $3d_{5/2}$ peak are used, as shown in Figure S61-63 for the photoelectron emission angles (0-75°). The effective attenuation length (EAL) of I $3d_{5/2}$ line is estimated by the NIST EAL13 database[9], adapting the PMMA density of 1.18 g/cm^3 and number of valence electrons counting from the monomer, assuming the amorphous thin film identical to bulk. The thicknesses of 500, 3000 and 6000 rpm PMMA thin films are estimated to be 3.8, 2.1, 1.7 nm, respectively.

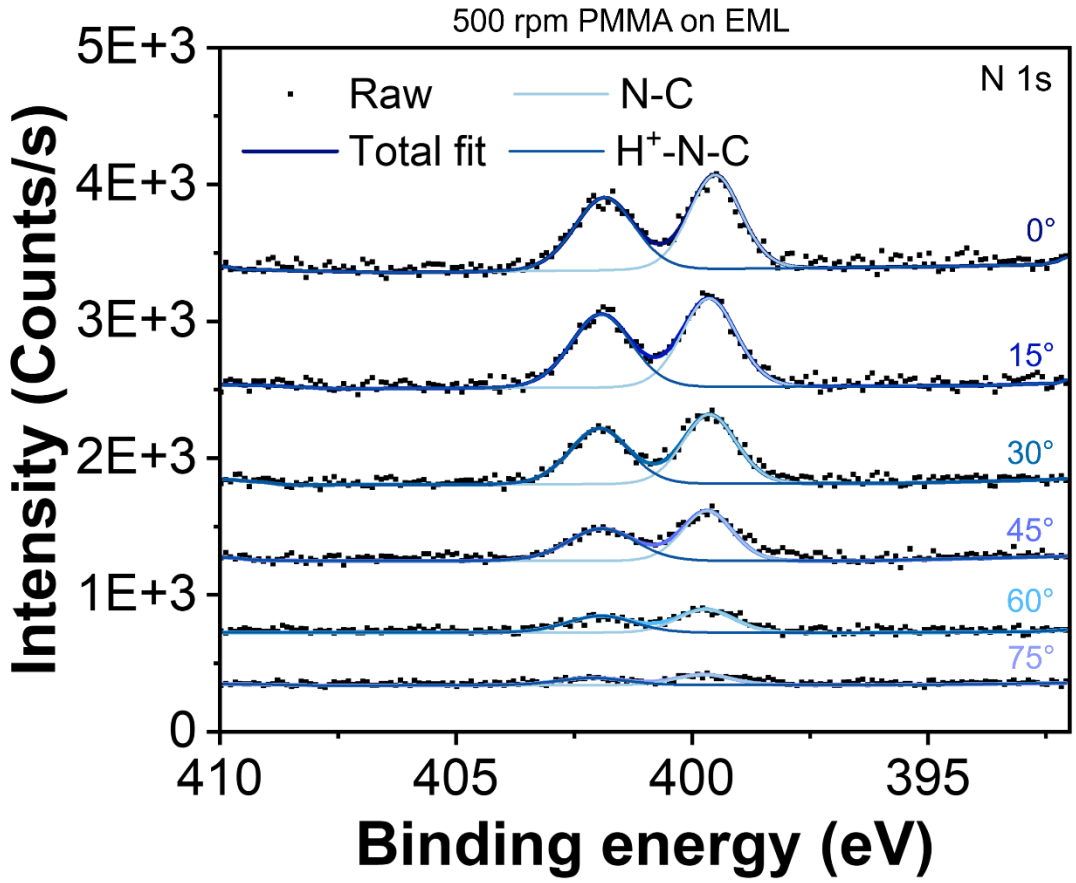

Fig. S52. ARXPS N1s spectra of a 500 rpm PMMA thin film on CuI(*Hda*).

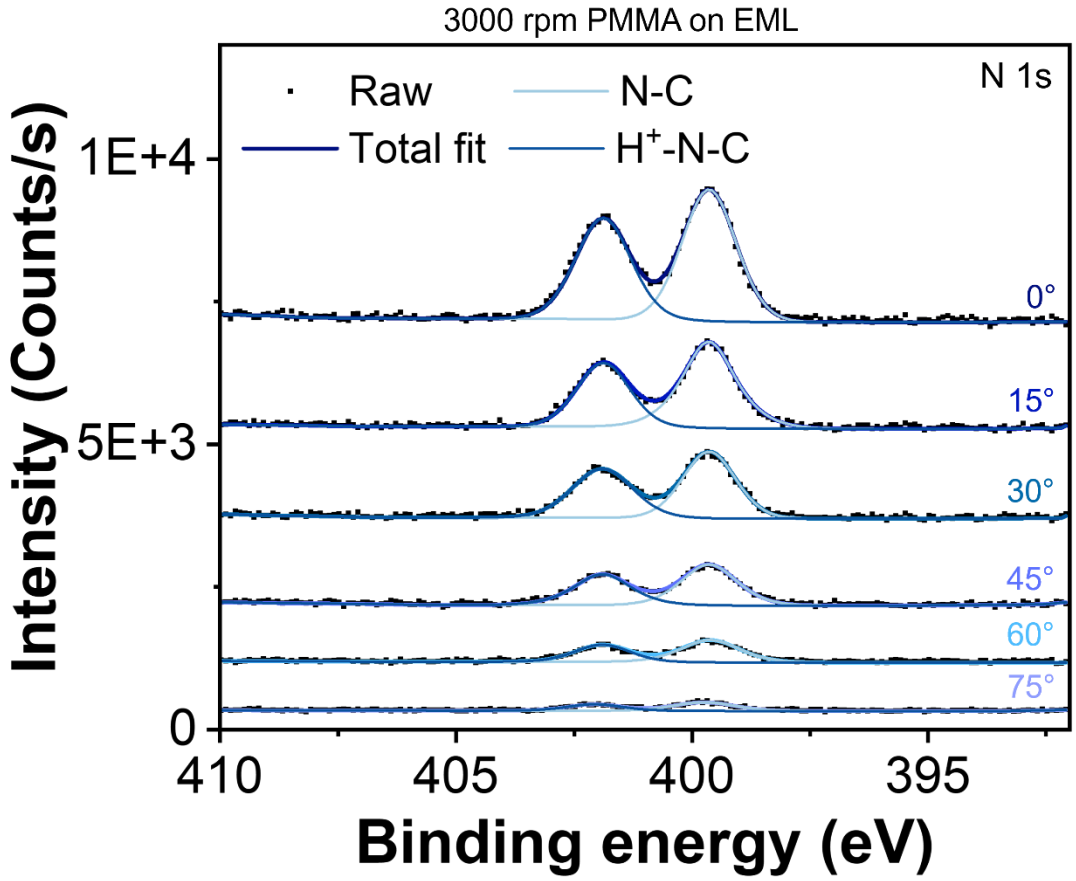

Fig. S53. ARXPS N1s spectra of a 3000 rpm PMMA thin film on CuI(*Hda*).

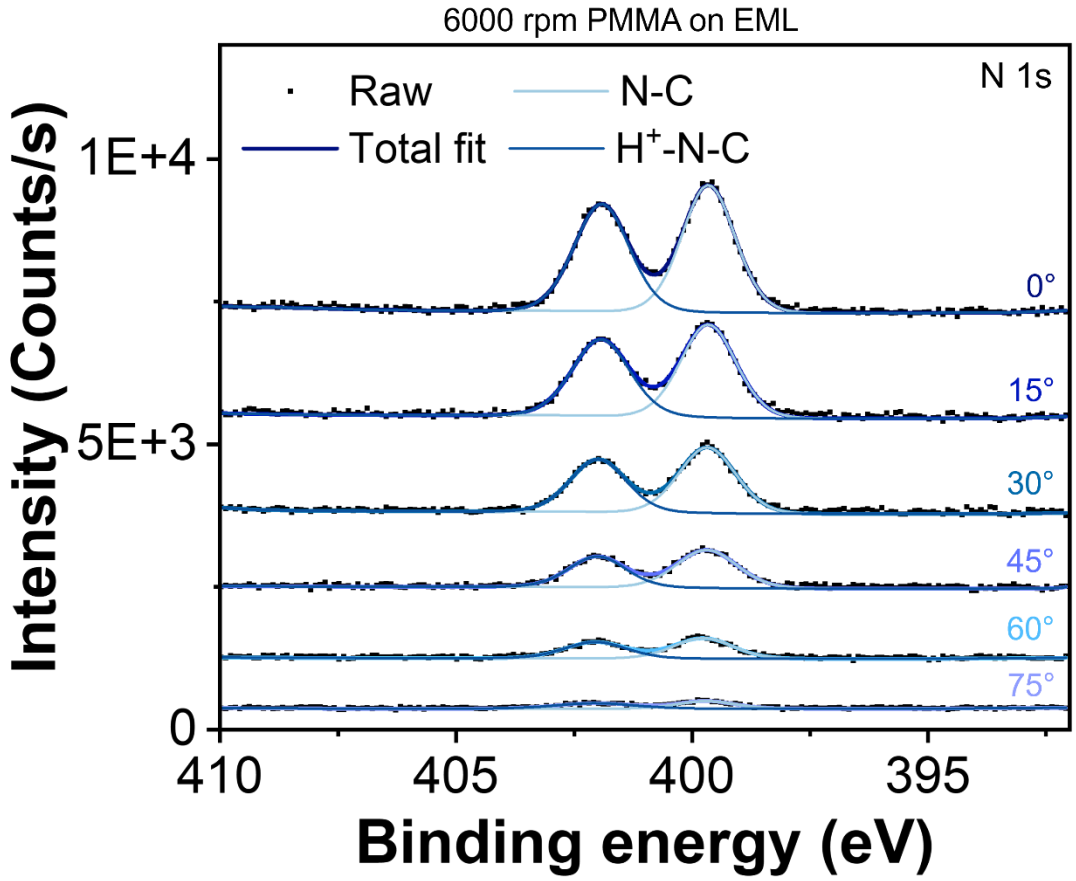

Fig. S54. ARXPS N1s spectra of a 6000 rpm PMMA thin film on CuI(*Hda*).

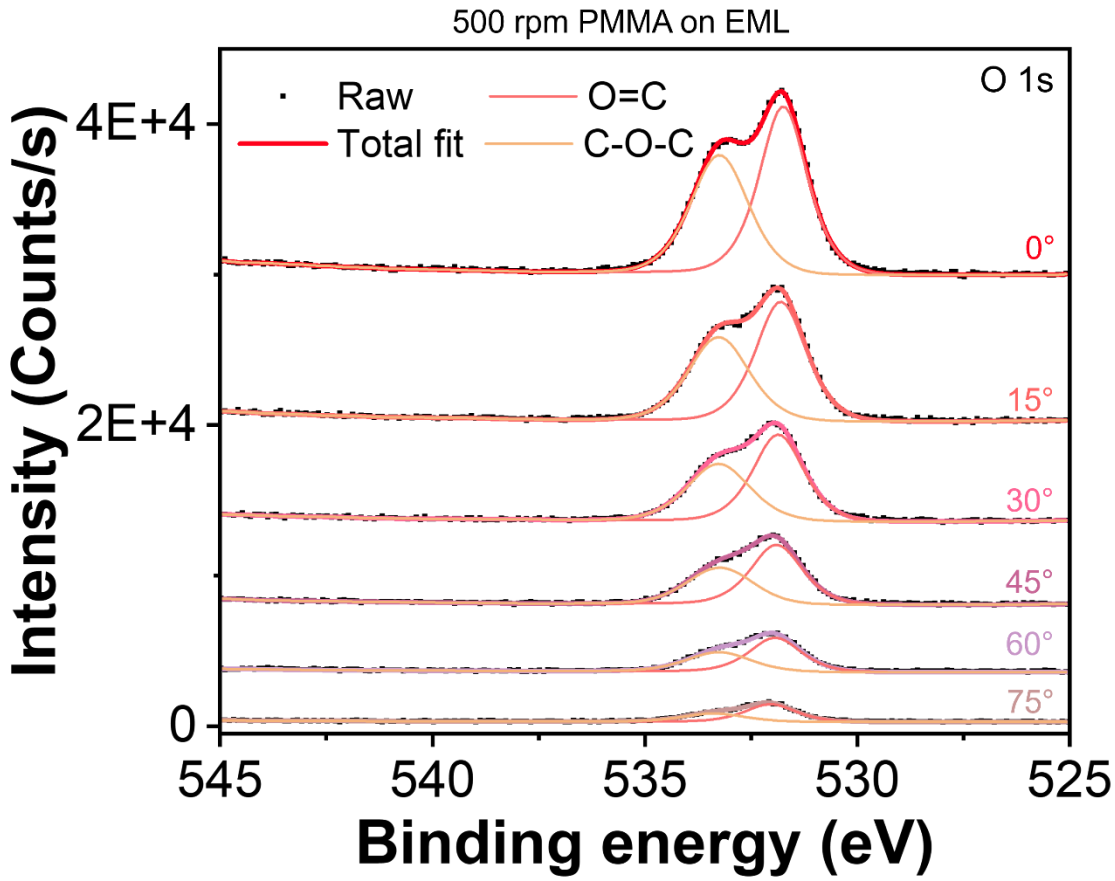

Fig. S55. ARXPS O1s spectra of a 500 rpm PMMA thin film on CuI(*Hda*).

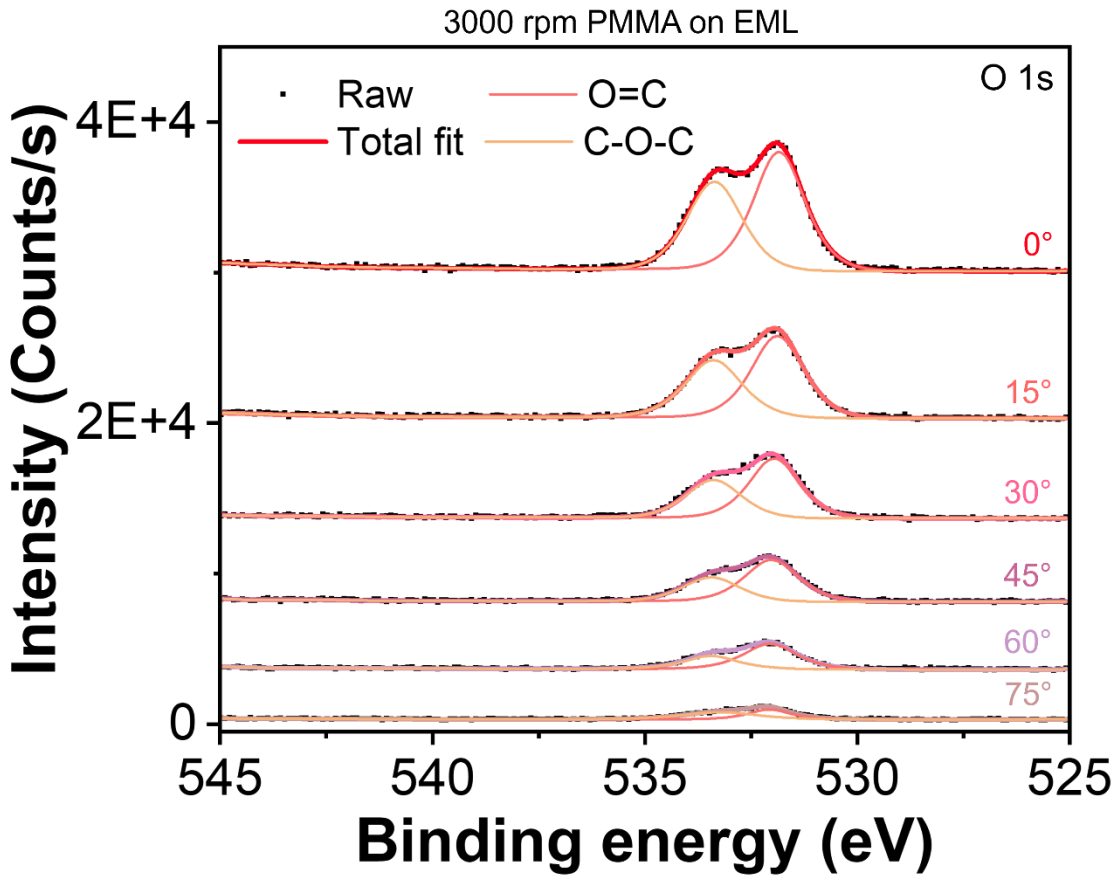

Fig. S56. ARXPS O1s spectra of a 3000 rpm PMMA thin film on CuI(*Hda*).

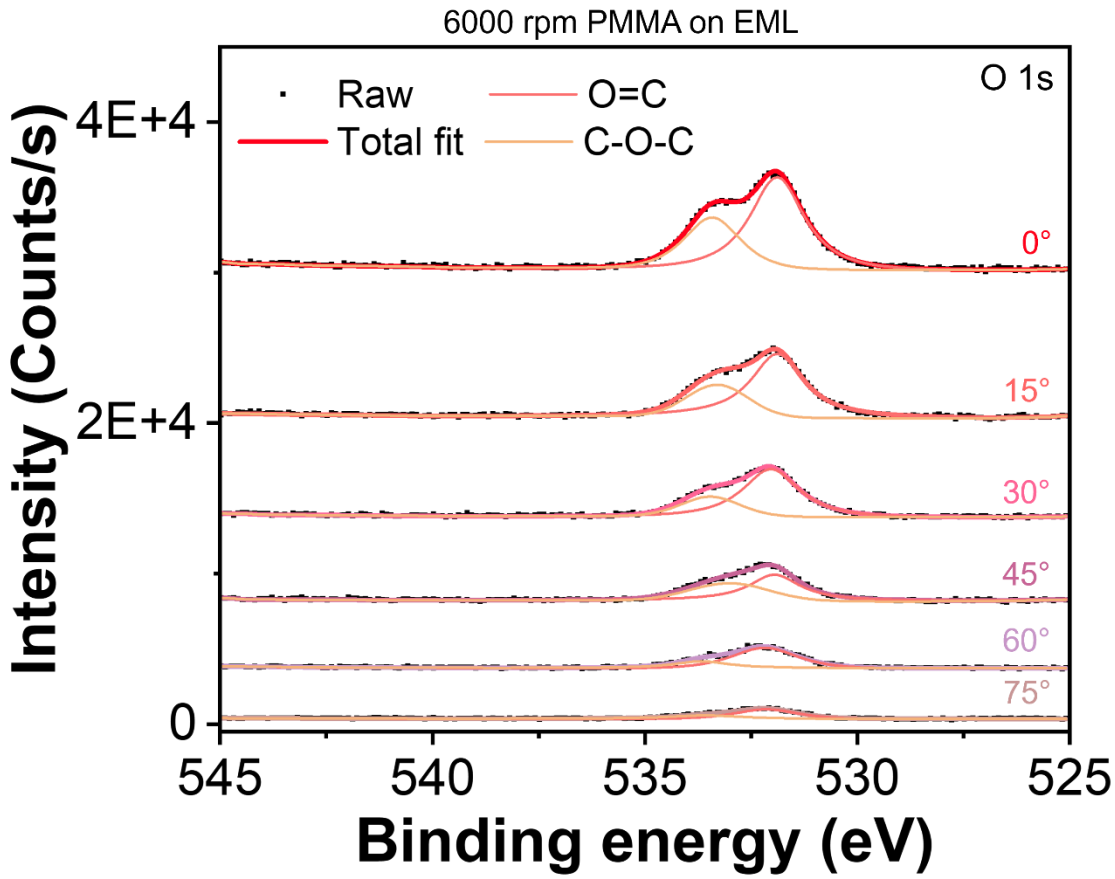

Fig. S57. ARXPS O1s spectra of a 6000 rpm PMMA thin film on CuI(*Hda*).

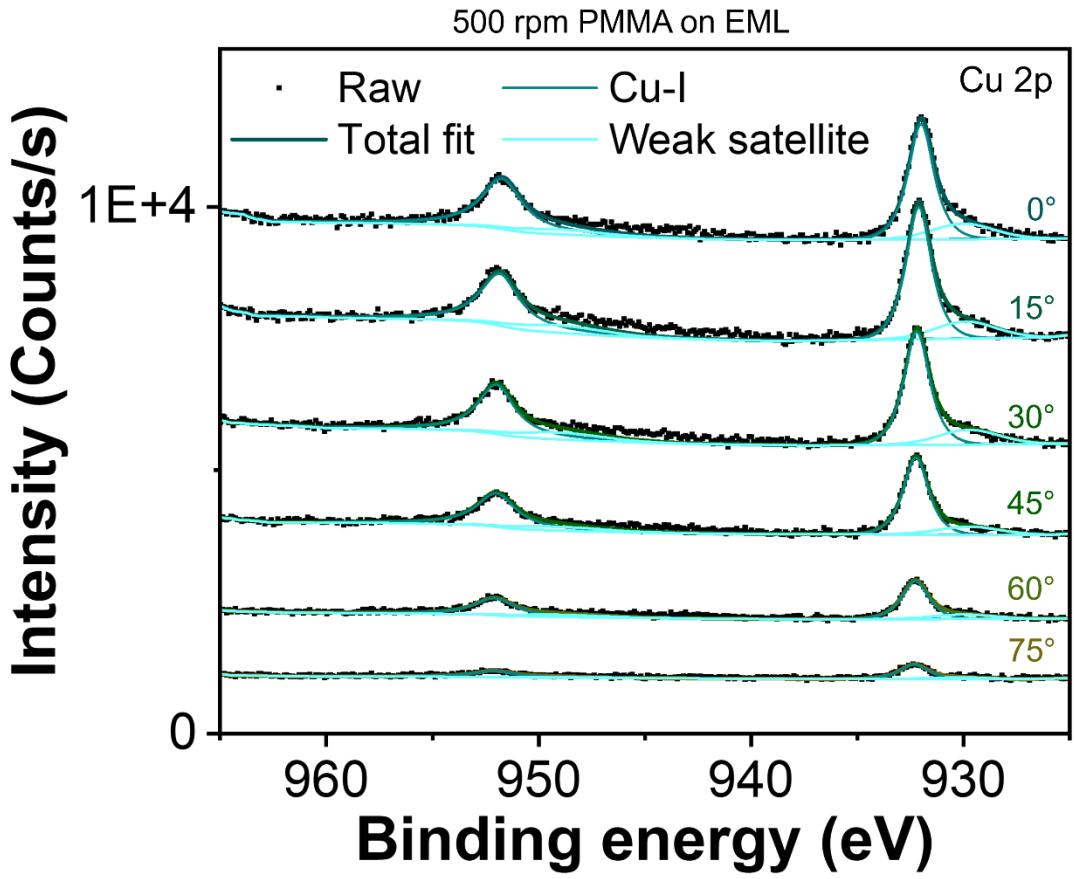

Fig. S58. ARXPS Cu2p spectra of a 500 rpm PMMA thin film on CuI(*Hda*).

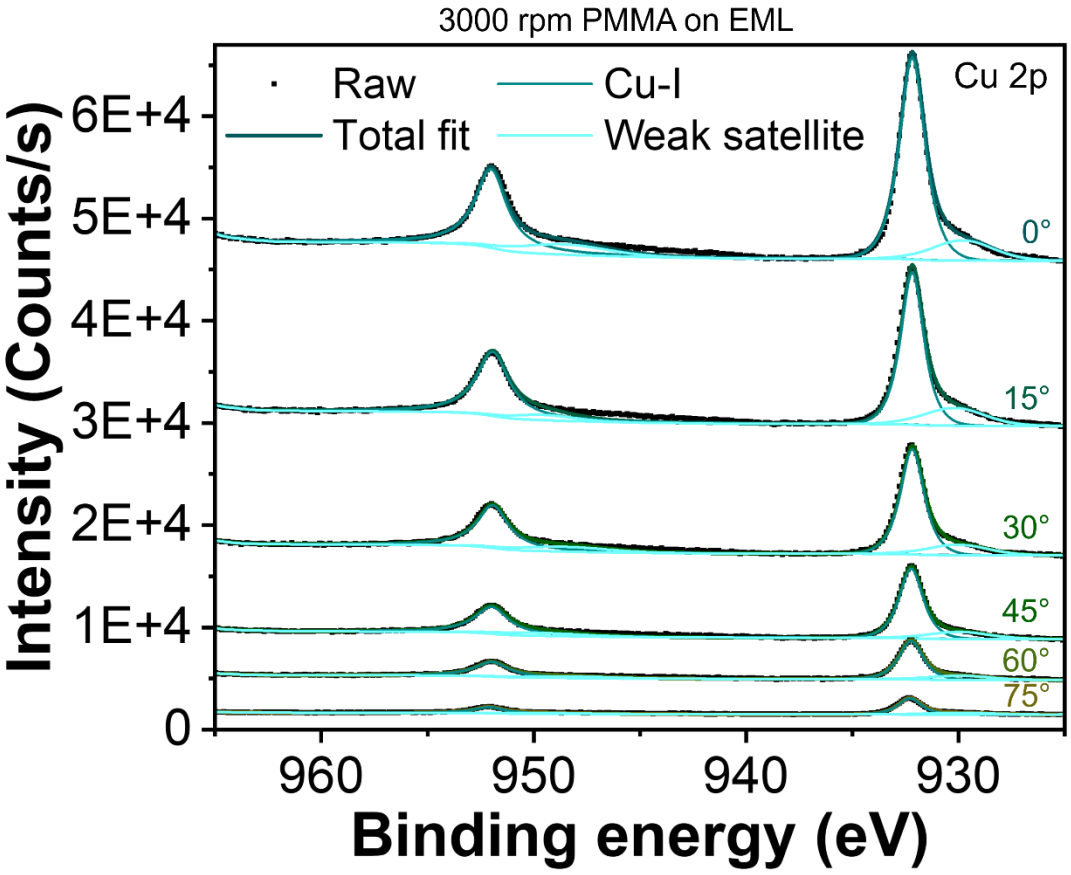

Fig. S59. ARXPS Cu2p spectra of a 3000 rpm PMMA thin film on CuI(*Hda*).

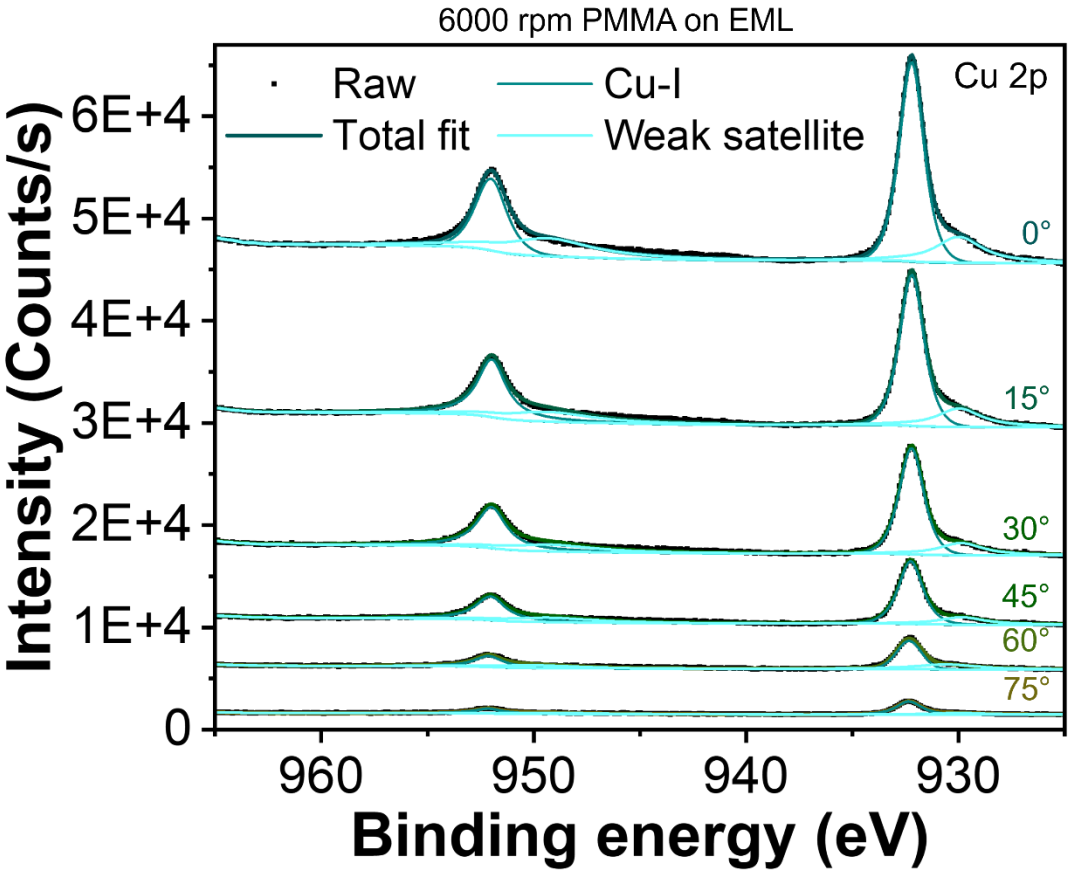

Fig. S60. ARXPS Cu2p spectra of a 6000 rpm PMMA thin film on CuI(*Hda*).

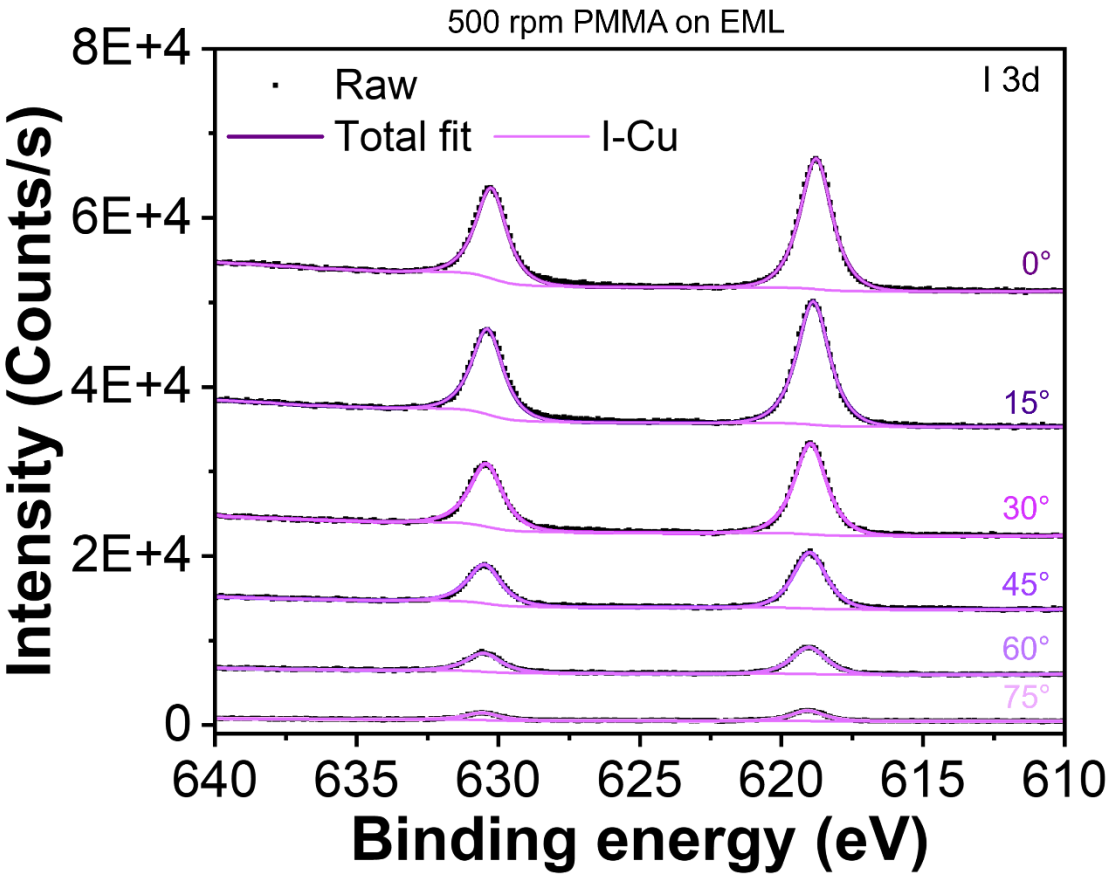

Fig. S61. ARXPS I3d spectra of a 500 rpm PMMA thin film on CuI(*Hda*).

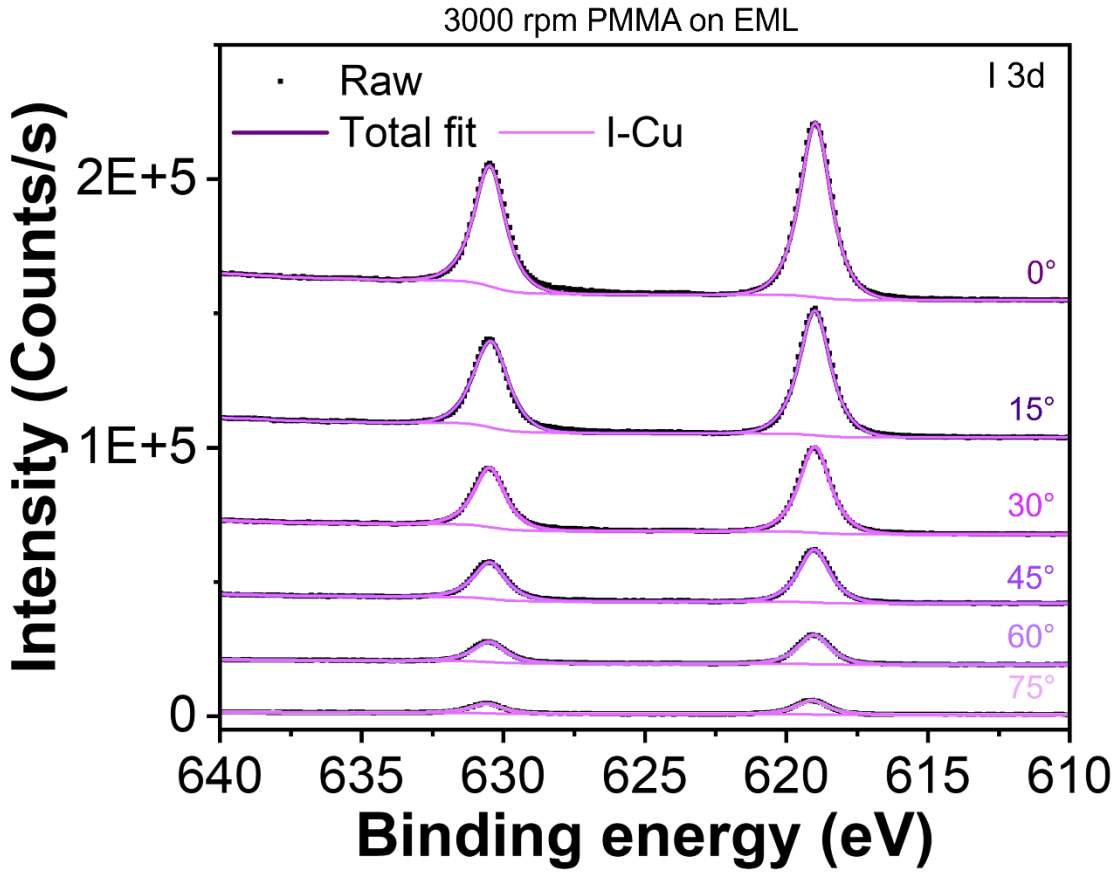

Fig. S62. ARXPS I3d spectra of a 3000 rpm PMMA thin film on CuI(*Hda*).

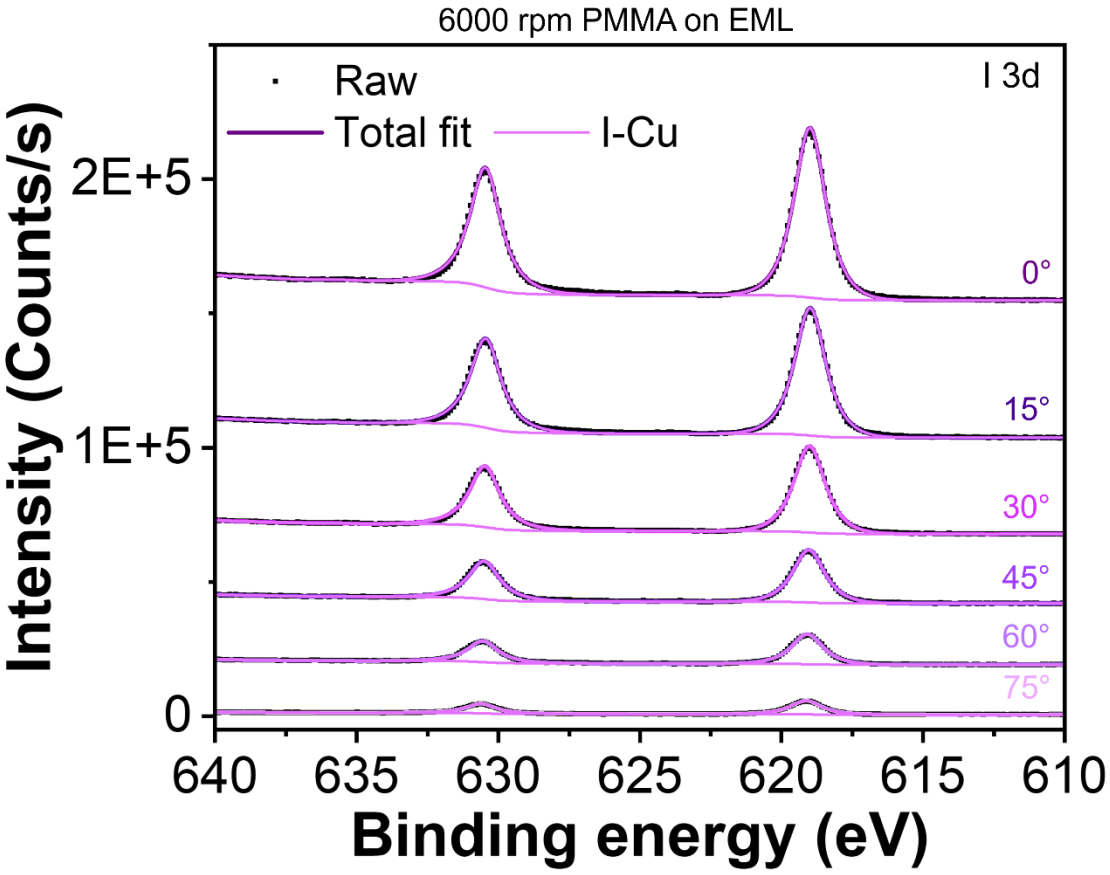

Fig. S63. ARXPS I3d spectra of a 6000 rpm PMMA thin film on CuI(*Hda*).

Summary of the device performance and reported metal halide-based blue LEDs

Table S8. Summary of the device performance of metal halide-based blue LEDs

Emission materials	Pb-free (Y/N)	λ_{max} (nm)	EQE (%)	T_{50} (min)	Ref
1D-Cu_4I_8(*Hdabco*)$_4$	Y	450	12.57	12240 (encapsulated) 6780	This work
$Cs_3Cu_2I_5$ NCs	Y	445	1.12	6480	[10]
$TEA_2Cu_2Br_4$	Y	463	0.11	-	[11]
$CsPbBr_3$ QDs	N	465	10.3	18	[12]
$CsPbBr_3$ c-NCs	N	463	11.9	17	[13]
$PEA_2A_{n-1}Pb_nX_{3n+1}$	N	490	1.5	10	[14]
$CsPbBr_3$ nanoplatelets	N	489	0.55	NA	[15]
PBABry($Cs_{0.7}FA_{0.3}PbBr_3$)	N	483	9.5	4.17	[16]
$CsPbCl_xBr_{3-x}$	N	480	5.7	10	[17]
$PEA_2(CsPbBr_3)_2PbBr_4$	N	488	12.1	NA	[18]
PEACl:$CsPbBr_3$:YCl_3	N	477	11	120	[19]
$CsPbBr_3$ QWs	N	478	6.3	2.5	[20]
$CsPbCl_xBr_{3-x}$ NCs	N	470	1.34	4.3	[21]
$CsPbCl_xBr_{3-x}$ NCs	N	470	0.86	~1	[22]
$(Rb_{0.33}Cs_{0.67})FA_{0.58}PbCl_{1.25}Br_{1.75}$	N	466	0.61	NA	[23]
$CsPbBr_3$ nanoplatelets	N	464	0.3	NA	[15]
$CsPbBr_3$	N	464	0.11	NA	[24]
$CsPb(Br/Cl)_3$	N	463	1	4	[25]
$CsPb(Br_{0.61}Cl_{0.39})_3$	N	462	1.03	NA	[26]
$CsPbBr_3$ QD	N	470	12.3	20	[27]
$CsPbBr_3$	N	459	0.3	NA	[28]
$FAPbBr_3$ nanoplatelets	N	439	0.14	NA	[29]
PBA_2PbBr_4	N	436	0.04	1	[30]
PBA_2PbBr_4	N	461	2	1	[30]
$CH_3NH_3PbBr_3$	N	432	2.31	NA	[31]
2D-$(PEA)_2PbBr_4$	N	408	0.31	>1350	[32]

p-PDAPbBr$_4$	N	465	2.6	13.5	33
PEA$_2$(Pb$_x$Cs$_{1-x}$)$_{n-1}$Pb$_n$Br$_{3n+1}$	N	454	1.35	14.5	34
BI$_2$PbBr$_4$	N	449	3.08	210	35
PEA$_2$(Cs$_x$EA$_{1-x}$PbBr$_3$)$_{n-1}$PbBr$_4$	N	486	9.06	NA	36
CsCl-PEA$_2$(Cs$_x$EA$_{1-x}$PbBr$_3$)$_{n-1}$PbBr$_4$	N	486	16.07	0.083	36
PPNCl-CsPbBr$_x$Cl$_{3-x}$	N	483 474 464	21.4 13.2 7.3	129	37

Supplementary note 8. Thermal and long-term stability of CuI(*Hda*)

Thermogravimetric analyses (TGA) of CuI(*Hda*) were performed on powder samples using the TA Instrument Q5000IR thermalgravimetric analyzer to investigate the thermal stability. The nitrogen flow and sample purge rate are at 10 and 12 mL/min, respectively. About 3 mg of samples were loaded onto a platinum sample pan and heated from room temperature to 450 °C at a rate of 10 °C/min under nitrogen flow.

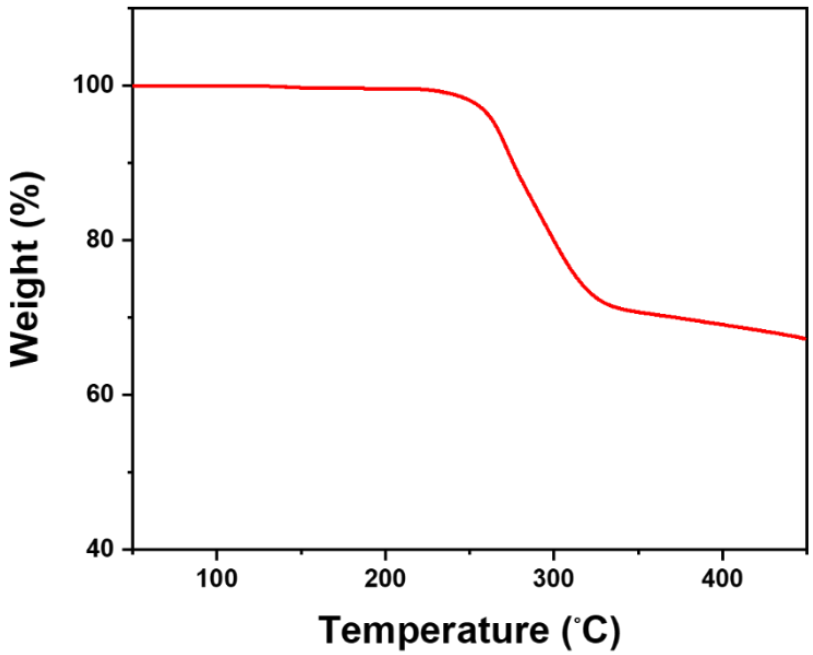

Fig. S64. Thermogravimetric (TG) profile of CuI(*Hda*).

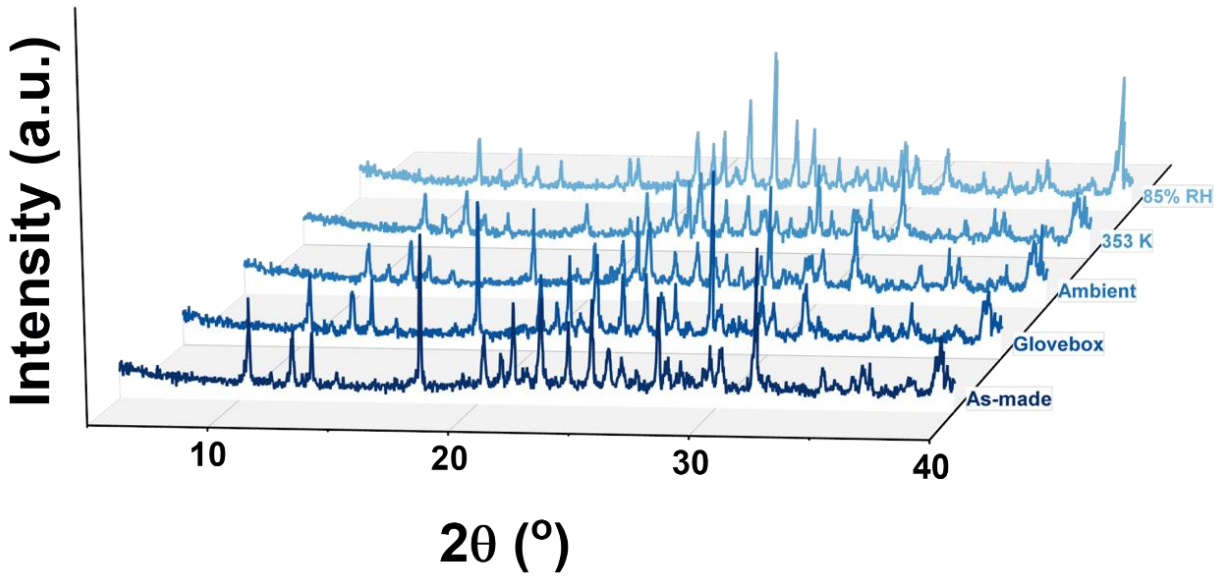

Fig. S65. PXRD patterns showing long-term stability of CuI(*Hda*) powders upon exposure to various conditions for 180 days.

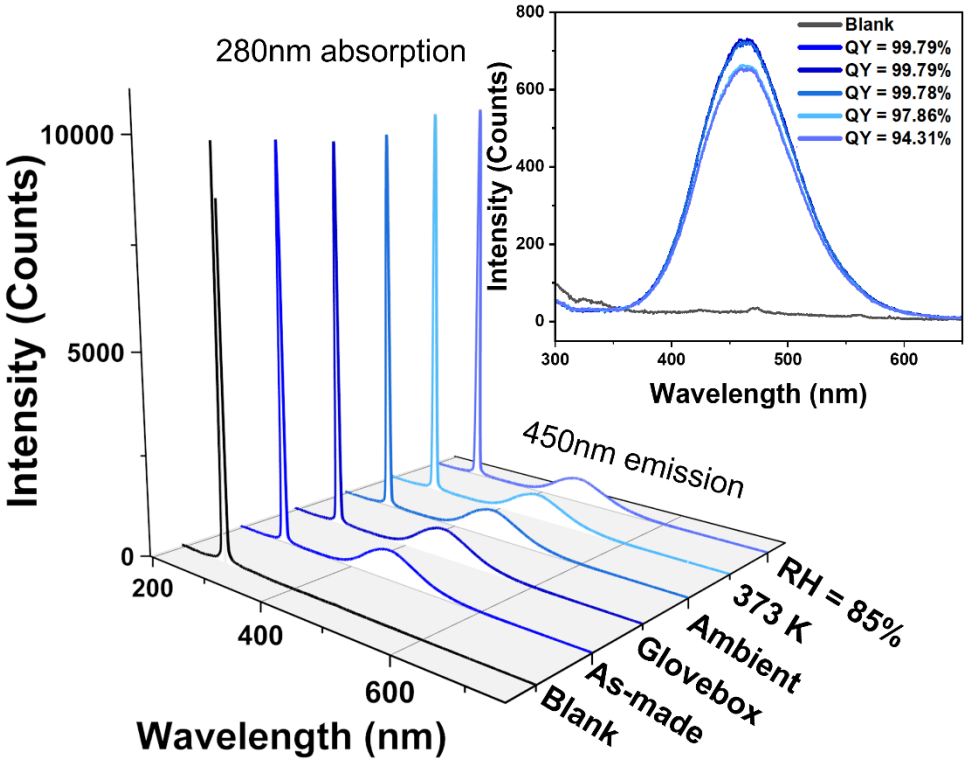

Fig. S66. PLQY evolution of CuI(*Hda*) thin films upon exposure to various conditions for 180 days.

References

1 Reger, D. *et al.* A Family of Superhelicenes: Easily Tunable, Chiral Nanographenes by Merging Helicity with Planar π Systems. *Angewandte Chemie International Edition* **60**, 18073-18081, doi:https://doi.org/10.1002/anie.202103253 (2021).

2 Louillat, M.-L. & Patureau, F. W. Toward Polynuclear Ru–Cu Catalytic Dehydrogenative C–N Bond Formation, on the Reactivity of Carbazoles. *Organic Letters* **15**, 164-167, doi:10.1021/ol303216u (2013).

3 Rowland, C. A., Yap, G. P. A. & Bloch, E. D. Novel syntheses of carbazole-3,6-dicarboxylate ligands and their utilization for porous coordination cages. *Dalton Transactions* **49**, 16340-16347, doi:10.1039/D0DT01149E (2020).

4 Tang, X. *et al.* Nona- and undecanuclear nickel phosphonate cages. *Inorganica Chimica Acta* **439**, 77-81, doi:https://doi.org/10.1016/j.ica.2015.10.003 (2016).

5 Lin, Y. *et al.* Self-Assembled Monolayer Enables Hole Transport Layer-Free Organic Solar Cells with 18% Efficiency and Improved Operational Stability. *ACS Energy Letters* **5**, 2935-2944, doi:10.1021/acsenergylett.0c01421 (2020).

6 Paniagua, S. A., Li, E. L. & Marder, S. R. Adsorption studies of a phosphonic acid on ITO: film coverage, purity, and induced electronic structure changes. *Physical Chemistry Chemical Physics* **16**, 2874-2881, doi:10.1039/C3CP54637C (2014).

7 Seah, M. P. Simple universal curve for the energy-dependent electron attenuation length for all materials. *Surface and Interface Analysis* **44**, 1353-1359, doi:https://doi.org/10.1002/sia.5033 (2012).

8 Hanson, E. L., Schwartz, J., Nickel, B., Koch, N. & Danisman, M. F. Bonding Self-Assembled, Compact Organophosphonate Monolayers to the Native Oxide Surface of Silicon. *Journal of the American Chemical Society* **125**, 16074-16080, doi:10.1021/ja035956z (2003).

9 Jablonski, A. & Powell, C. *NIST Electron Effective-Attenuation-Length Database*, National Institute of Standards and Technology Gaithersburg, (2011).

10 Wang, L. *et al.* Colloidal synthesis of ternary copper halide nanocrystals for high-efficiency deep-blue light-emitting diodes with a half-lifetime above 100 h. *Nano Letters* **20**, 3568-3576 (2020).

11 Liu, X. *et al.* Near-unity blue luminance from lead-free copper halides for light-emitting diodes. *Nano Energy* **91**, 106664, doi:https://doi.org/10.1016/j.nanoen.2021.106664 (2022).

12 Jiang, Y. *et al.* Synthesis-on-substrate of quantum dot solids. *Nature* **612**, 679-684, doi:10.1038/s41586-022-05486-3 (2022).

13 Wang, Y.-K. *et al.* Self-assembled monolayer–based blue perovskite LEDs. *Science Advances* **9**, eadh2140, doi:doi:10.1126/sciadv.adh2140 (2023).
14 Xing, J. *et al.* Color-stable highly luminescent sky-blue perovskite light-emitting diodes. *Nature communications* **9**, 3541 (2018).
15 Hoye, R. L. *et al.* Identifying and reducing interfacial losses to enhance color-pure electroluminescence in blue-emitting perovskite nanoplatelet light-emitting diodes. *ACS Energy Letters* **4**, 1181-1188 (2019).
16 Liu, Y. *et al.* Efficient blue light-emitting diodes based on quantum-confined bromide perovskite nanostructures. *Nature Photonics* **13**, 760-764 (2019).
17 Li, Z. *et al.* Modulation of recombination zone position for quasi-two-dimensional blue perovskite light-emitting diodes with efficiency exceeding 5%. *Nature communications* **10**, 1027 (2019).
18 Chu, Z. *et al.* Large cation ethylammonium incorporated perovskite for efficient and spectra stable blue light-emitting diodes. *Nature Communications* **11**, 4165 (2020).
19 Wang, Q. *et al.* Efficient sky-blue perovskite light-emitting diodes via photoluminescence enhancement. *Nature communications* **10**, 5633 (2019).
20 Wang, Y.-K. *et al.* Chelating-agent-assisted control of CsPbBr3 quantum well growth enables stable blue perovskite emitters. *Nature communications* **11**, 3674 (2020).
21 Shin, Y. S. *et al.* Functionalized PFN-X (X= Cl, Br, or I) for balanced charge carriers of highly efficient blue light-emitting diodes. *ACS applied materials & interfaces* **12**, 35740-35747 (2020).
22 Shin, Y. S. *et al.* Vivid and fully saturated blue light-emitting diodes based on ligand-modified halide perovskite nanocrystals. *ACS applied materials & interfaces* **11**, 23401-23409 (2019).
23 Meng, F. *et al.* Incorporation of rubidium cations into blue perovskite quantum dot light-emitting diodes via FABr-modified multi-cation hot-injection method. *Nanoscale* **11**, 1295-1303 (2019).
24 Todorović, P. *et al.* Spectrally tunable and stable electroluminescence enabled by rubidium doping of CsPbBr3 nanocrystals. *Advanced Optical Materials* **7**, 1901440 (2019).
25 Ochsenbein, S. T., Krieg, F., Shynkarenko, Y., Rainò, G. & Kovalenko, M. V. Engineering color-stable blue light-emitting diodes with lead halide perovskite nanocrystals. *ACS applied materials & interfaces* **11**, 21655-21660 (2019).
26 Shynkarenko, Y. *et al.* Direct synthesis of quaternary alkylammonium-capped perovskite nanocrystals for efficient blue and green light-emitting diodes. *ACS energy letters* **4**, 2703-2711 (2019).
27 Dong, Y. *et al.* Bipolar-shell resurfacing for blue LEDs based on strongly

confined perovskite quantum dots. *Nature nanotechnology* **15**, 668-674 (2020).
28 Shi, S., Wang, Y., Zeng, S., Cui, Y. & Xiao, Y. Surface Regulation of CsPbBr3 Quantum Dots for Standard Blue‐Emission with Boosted PLQY. *Advanced Optical Materials* **8**, 2000167 (2020).
29 Peng, S. *et al.* Effective surface ligand-concentration tuning of deep-blue luminescent FAPbBr3 nanoplatelets with enhanced stability and charge transport. *ACS applied materials & interfaces* **12**, 31863-31874 (2020).
30 Yantara, N. *et al.* Designing the perovskite structural landscape for efficient blue emission. *ACS Energy Letters* **5**, 1593-1600 (2020).
31 Kumar, S. *et al.* Efficient blue electroluminescence using quantum-confined two-dimensional perovskites. *Acs Nano* **10**, 9720-9729 (2016).
32 Deng, W. & Jin, X. Y. lv, X. Zhang, X. Zhang and J. Jie. *Adv. Funct. Mater* **29**, 1903861 (2019).
33 Yuan, S. *et al.* Optimization of low‐dimensional components of quasi‐2D perovskite films for deep‐blue light‐emitting diodes. *Advanced Materials* **31**, 1904319 (2019).
34 Jiang, Y. *et al.* Spectra stable blue perovskite light-emitting diodes. *Nature communications* **10**, 1868 (2019).
35 Lin, Z. *et al.* Deep blue photoluminescence and optical gain from sodium-doped carbon dots. *Journal of Luminescence* **246**, 118856 (2022).
36 Chu, Z. *et al.* Blue light-emitting diodes based on quasi-two-dimensional perovskite with efficient charge injection and optimized phase distribution via an alkali metal salt. *Nature Electronics* **6**, 360-369, doi:10.1038/s41928-023-00955-7 (2023).
37 Yuan, S. *et al.* Efficient blue electroluminescence from reduced-dimensional perovskites. *Nature Photonics*, doi:10.1038/s41566-024-01382-6 (2024).